Starshade Technology Development Activity Milestone 3:

Demonstration of Solar Glint Lobe Scatter Performance

Evan Hilgemann, Stuart Shaklan, Dylan McKeithen, Douglas Lisman, Stefan Martin, David Webb, Nicholas Saltarelli, Maxwell Ferguson, and John Steeves

Jet Propulsion Laboratory, California Institute of Technology, 4800 Oak Grove Dr., Pasadena, CA, USA 91109

November 15, 2019

Contents

Executive Summary

We report the results of Milestone 3 experiments for the Exoplanet Exploration Program Starshade Technology Activity (S5). The goal of this milestone is to demonstrate through experiment and analysis that solar glint from optical edge segments having undergone thermal and deployment cycles remains fainter than visual magnitude V=25 for the WFIRST Starshade Rendezvous Mission (SRM) and HabEx starshade missions.

Prototype optical edge segments were assembled from 500 mm long, chemically-etched amorphous metal strips bonded to carbon fiber composite substrates. The working edge is sharp with a radius of curvature of ~150 nm. Segments are shaped with a curvature approximating an SRM petal.

A custom scatterometer was built to measure the scatter at a fixed angle along the length of the edge segments. Data from the scatterometer were combined with data from a separate multi-angle scatterometer that measures the full angular scatter profile from 50 mm long edge coupons.

Together, these instruments when combined with a starshade imaging analysis toolkit, show that after thermal and deployment cycles, the average level of scatter from the segments at the inner working angle is fainter than V=25 at the 95% confidence level, except for sun angles > 78° in the SRM band 615-800 nm. The optical performance was not adversely affected by thermal and deployment cycles. Methods to decrease the solar glint brightness by a factor of 10 are discussed.

1 Introduction

This report presents the S5 efforts to verify solar glint performance (KPP3) and is intended to close technology Milestone 3, which reads:

Optical edge segments demonstrate scatter performance consistent with solar glint lobes fainter than visual magnitude 25 after relevant thermal and deploy cycles.

This specification applies over the full range of wavelengths and star-sun angles for the WFIRST Starshade Rendezvous Mission (SRM) and the HabEx Mission (Table 1).

Solar glint lobes are regions of mostly specular reflections and diffraction from optical edges (OE) oriented normal to the Sun-Starshade-Telescope plane. The lobes appear in marginally resolved spots mostly contained within the inner working angle (IWA) defined as the angle from the center to the tips of the starshade as seen from the telescope. The impact of these lobes on detection performance is not straightforward to evaluate. Since we do not know the planet position *a priori*, and since most of the light in the glint lobes does not impact planet detection, the relevant lobe brightness metric is the azimuthally averaged brightness at and beyond the IWA. Here we report on the solar glint performance as the 95% confidence interval of the azimuthal average of the brightness at the IWA. Our results are based on experimental measurements of scatter from prototype optical edge segment assemblies that have undergone extensive thermal and deployment cycles.

Table 1: Starshade Missions

Mission	Bandpass	Starshade Diam.	Distance	Star-Sun Angle
SRM ('blue')	425-552 nm	26 m	37.2 Mm	54° - 83°
SRM ('green')	615-800 nm	26 m	25.7 Mm	54° - 83°
HabEx	300-1000 nm	52 m	76 Mm	40° - 83°

Section 2 describes the appearance of the glint lobes and the physics behind them.

Section 3 details two custom scatterometers and how they are used to measure edge segment optical performance and to predict flight performance. One is a multi-angle scatterometer (MAS) used to measure the scatter properties of 50 mm long edge coupons over a 3 mm wide spot-size. The other is a single-angle scatterometer (SAS) used to measure the scatter along 500 mm long edge segments and 50 mm long coupons over their full lengths. The segment-to-coupon scatter ratio is computed and used in conjunction with the MAS data in the analysis of glint lobe brightness.

Section 4 describes the flight OE design with approximately 1,000 mm long edge segments that consist of a photochemically etched amorphous metal (AM) working edge bonded to a carbon fiber reinforced polymer (CFRP) substrate. The etching process creates a sharp terminal edge that both limits solar glint and defines the precise in-plane shape. In-plane shape is not a metric for this milestone, but is a petal level requirement that has been characterized (see Appendix A).

Section 4 also describes the OE prototypes used as MS3 test articles. A preliminary AM-CFRP bonding process resulted in sub-optimal adhesion and allowed excess epoxy to flow onto the terminal edge. There are noticeable local increases to OE segment scatter that

are hypothesized to be either residual cured epoxy or damage from removing uncured epoxy during assembly. An ongoing effort is developing an improved OE bonding process that will ultimately be verified as part of MS 5b.

Section 5 presents the relevant environments, test levels and margins. TRL-5 is defined at the OE segment level with relevant environments of thermal and deploy cycles (Section 2.1.7 of the S5 Technology Plan[1]). OE segments will be electrically grounded to the petal assembly and spacecraft to preclude discharge events. The TRL-6 relevant environments will expand to include dust, space charging and launch vibration. There are no anticipated problems with performance in all operational environments.

Optical test data for both coupons and segments are reported in Section 6. Section 7 presents the detailed error analysis and derives the model uncertainty factor (MUF) for 95% confidence. Milestone compliance is addressed by estimating glint lobe magnitudes for the relevant wavelength bands and solar angles. Overall performance is within milestone specification for all bands and solar angles with 95% confidence, with the exception of the solar angle range of 78°-83° in the SRM green band, where the average lobe magnitude is slightly brighter than V=25. This is followed by a discussion of the implications to mission performance at these levels of solar glint. The section also includes a discussion of glint lobe brightness mitigation approaches. Conclusions are presented in Section 8. Finally, Appendices A-E provide details on in plane shape testing, stowed testing, a table of the segment test sequences, and plots of segment and coupon scatter test results generated by the SAS.

2   Solar Glint

2.1   Glint on the Starshade

A small fraction of sunlight will glint from the edge of the starshade into the telescope. Even with the vast distance of tens of thousands of kilometers, glint from the razor-sharp edges is the brightest source of instrument background. The observational geometry is shown in Figure 1. The sun is behind (on the target side of) the starshade so as not to illuminate the telescope-facing surface. While some of the starshade's edges can be shaded from the sun using structures on the target-facing side, any part of the edge whose normal is in the plane of the sun-starshade-telescope triangle and within 90° of the sun and telescope will scatter some light in the telescope's direction. For the WFIRST starshade, roughly 130 m of edge contributes to the glint, of which ∼10 m has a strong specular component.

Previous testing showed that small-radius edges exhibit superior performance to larger radius edges, including those with commercial ultra-black coatings.[2,3] The terminal edges are sub micron in radius and tend to be quite specular. With specular edges, those edges in the correct orientation 'broadside to the sun' will contribute most of the observed glint. While this localized glint is much brighter than one would observe with diffuse edges, it is also concentrated inward of the starshade's tips, as shown in Figure 2. In this example, which is based upon the measured scatter from amorphous metal edges, the sun is at $\phi = 63°$ (27° behind the plane of the page). Those parts of the starshade edge that are horizontal in the picture contribute most of the glint. The result is a two-lobed pattern, with each lobe

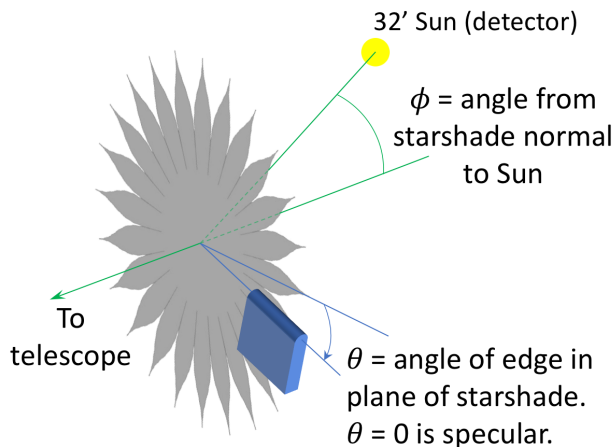only partially resolved at the resolution of the telescope.

Figure 1: Orientation of the sun, starshade, telescope, and a segment of optical edge that is glinting. The edge orientation angle is θ, and the sun angle is ϕ.

All of the sources of glint are internal to the nominal Inner Working Angle (IWA), defined as the angle to the outermost tip of the starshade. The wings of the telescope point spread function (PSF) are responsible for all of the glint at angles larger than the IWA. The total flux of each lobe, including the wings, is equivalent to a V=24-25 magnitude star depending on the starshade's distance and the wavelength, and of course the quality of the optical edges. In the WFIRST Starshade Rendezvous band of 615-800 nm, when the starshade is at a distance of 26 Mm, the integrated light of the lobes is about 2 magnitudes brighter than in the bluer band, 425-552 nm, where the separation is greater.

Planets are typically detected at the IWA and larger angles, in the wings of the glint lobes. About 40% of the glint light appears beyond the IWA. The process of detecting a planet requires analysis with a photometric aperture, *e.g.*, a simple circular aperture or a matched filter, and at the IWA this aperture will integrate light at angles centered on the IWA.

In the right panel of Figure 2 we show the equivalent magnitude within a photometric aperture with diameter λ/D where λ is the central wavelength in the bandpass and D is the telescope diameter (D=2.37 m for WFIRST). This image is the convolution of the starshade image on the left with a uniform circular aperture of diameter λ/D. The brightest point at the IWA is about 1 magnitude fainter than the integrated light of the glint, and the average light at the IWA within the photometric aperture is ≈ 0.8 magnitudes fainter than the peak. We will return to these points in the discussion of the results, Section 7.2. Note that the Johnson System of magnitudes is used throughout this document.

2.2 Glint Physics

We have developed and validated models to understand the nature of the scatter and guide the selection of edge shape, material, and radius. The first models we explored are described by McKeithen *et al*[5] and include: an analytical description of the field diffracted and reflected
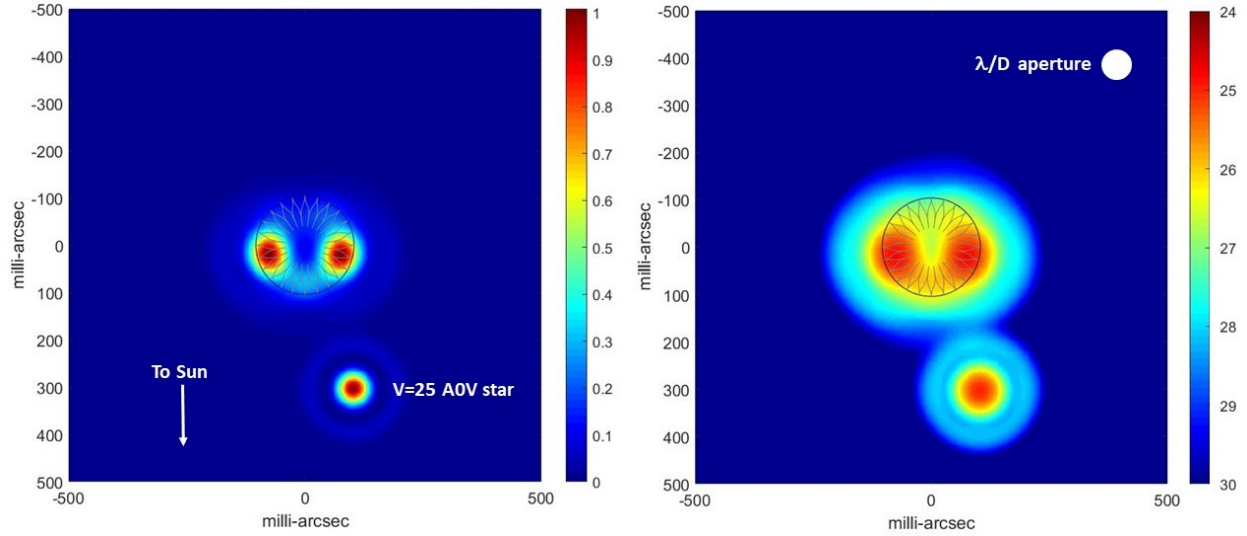
Figure 2: Left: Solar glint lobes are shown for the 26 m diameter WFIRST Rendezous starshade mission at a distance of 25.7 Mm, with bandpass 615-800 nm, and the sun 63° from the starshade normal (27° behind the plane of the page). For reference, a V=25 A0V star is also shown to the lower right; brightness scale is relative to the peak brightness of the star. The starshade is shown superimposed on the glint lobes. Right: the image has been convolved with an aperture 65 mas wide, equal to a photometric aperture of diameter λ/D at $\lambda = 710$ nm. This image shows the magnitude of the glint centered at any point, and integrated over the photometric aperture. The circle around the starshade is the IWA. This simulation was performed with the Starshade Imaging Simulation Tookit for Exoplanet Reconnaissance (SISTER) imaging package[4] using scatter data from an amorphous metal edge coupon.

by a cylinder-tipped half plane (a lollipop model); a finite-difference time domain (FDTD) model called Meep that solves Maxwell's equations in small temporal and spatial steps; and a combined diffraction and micro-facet reflection model (Modified Sommerfeld microfacet model, or MSμF) we developed to allow us to explore different radii, materials, and coatings. Recently, we have been using the commercial FDTD software Lumerical to model the performance of multi-layer coated edges (Section 7.2.2). Figure 3 shows a comparison of our models with a chemically etched amorphous metal edge coupon. The model predictions are in family with the measured data. Through the range of $40° - 60°$ the Lumerical prediction for amorphous metal underpredicts the measurements by 20-25%. The difference may be entirely attributable to the estimation error of the effective edge radius. The MSμF model is a better predictor, but it is not useful for the general case of a coated surface. The bottom-most curve shows the prediction for a 150 nm amorphous metal edge coated with a thin multi-layer hybrid interferometric/absorptive coating. This coating, which greatly reduces the scatter, even below the ideal diffraction limit, became available late in our study. We have additional discussion on this coating in Section 7.2.2.

The models explain the general ϕ dependence of the measured data which is nearly flat over the WFIRST operational range $54° < \phi < 83°$, and steeply increases at small angles where diffraction (the dashed black curve of Figure 3b) is dominant.
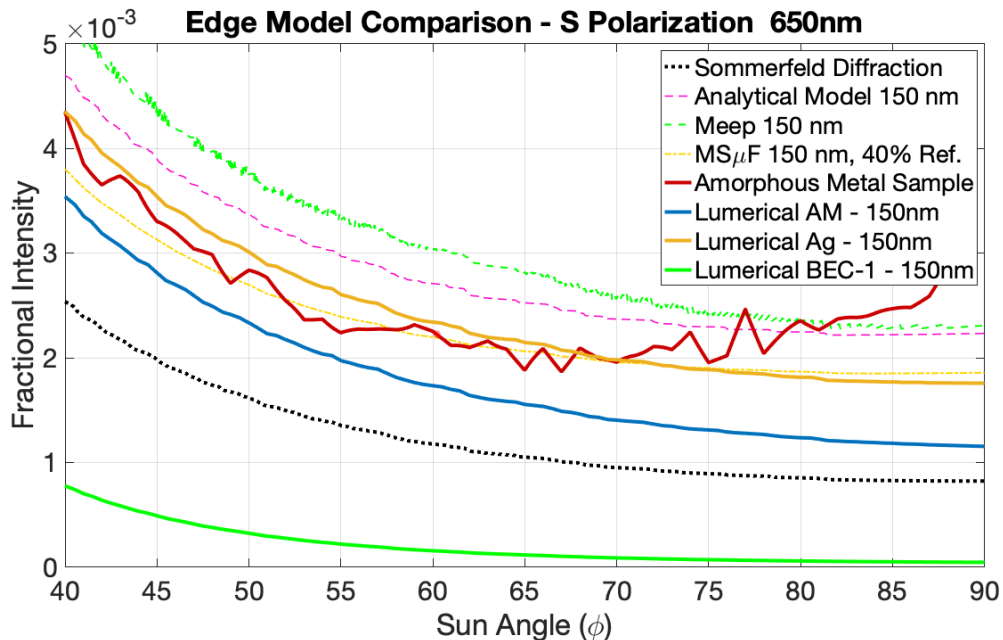

Figure 3: Model predictions vs. lab data for an amorphous metal edge. These data are for the dominant 'S' polarization which is parallel to the optical edge. The plot is scaled to show the fractional scatter in a collimated beam at a distance of 40 microns from the scattering edge. For a collimated beam, the fractional intensity for scatter from a straight edge scales linearly with distance.

Based upon these models, current and previous[6] measurements, and a host of mechanical factors, we adopted sharp, uncoated, amorphous metal edges as our baseline. These edges,

when etched to a radius of 100-200 nm, will scatter light to within a factor of 2 of the theoretical limit set by diffraction for a perfect conductor. In future work we will study the performance with a hybrid anti-reflection coating.

3 Measuring Glint in the Laboratory

We have built two instruments to measure the scatter function from optical edges. The first, the Multi-Angle Scatterometer, was built several years ago and measures the full 2-D scatter function[2] of ~50 mm long coupons. The second, the Single-Angle Scatterometer,[7] was built in 2018-2019 for Milestone 3 and measures over a fixed full-cone angle of ~30° along the 500 mm length of curved optical edge assemblies. In this section we briefly describe both instruments.

3.1 Multi-Angle Scatterometer

The MAS was designed to measure scatter performance of coupon scale (roughly 25 mm x 50 mm, Figure 4) components over the full range of possible sun angles. This measurement can

Figure 4: A 500 mm long optical edge segment. The amorphous metal edge is sandwiched between graphite composite substrates. Inset: an amorphous metal coupon mounted in its holder.

be used to test manufacturing methods or coatings before moving to larger components. The instrument has been more completely described elsewhere.[2] A general schematic and image is shown in Figure 5. To summarize, a collimated, calibrated 633 nm laser illuminates the terminal radius of an optical edge coupon that scatters light into a detector. The coupon and laser light can be rotated about two degrees of freedom to simulate the sun moving to different positions relative to the starshade. In both the MAS and Single-Angle Scatterometer (SAS), the source and detector are, for convenience of implementation, in the opposite sense to the sun and the telescope. This arrangement does not affect the range of angles explored.

The output of the MAS is effectively a heat map (Figure 6) that shows how an edge scatters light over any given angle. Information from the heat map can then be extracted to understand the scattered light characteristics of an entire starshade. Every pixel in the heatmap corresponds to a angle of the sun (vertical axis) and a position angle of the optical edge relative to the sun and telescope (horizontal axis), with specular reflection at 0°. The data from this map is the input to the scatter calculations in the SISTER simulations.

The long-term repeatability of the MAS (over several months) is the largest contributor to the Milestone 3 error budget. Measurements of the scatter of an amorphous metal coupon

between February and October 2019 had a standard deviation of 10%. It is possible that some of this is due to changes in both the position of the measurement along the edge, as well as changes in the edge itself (e.g. more or less clean). However, we are not able to separate those effects from the instrument itself and therefore use the measured repeatability of 10% in our estimation the MAS precision.
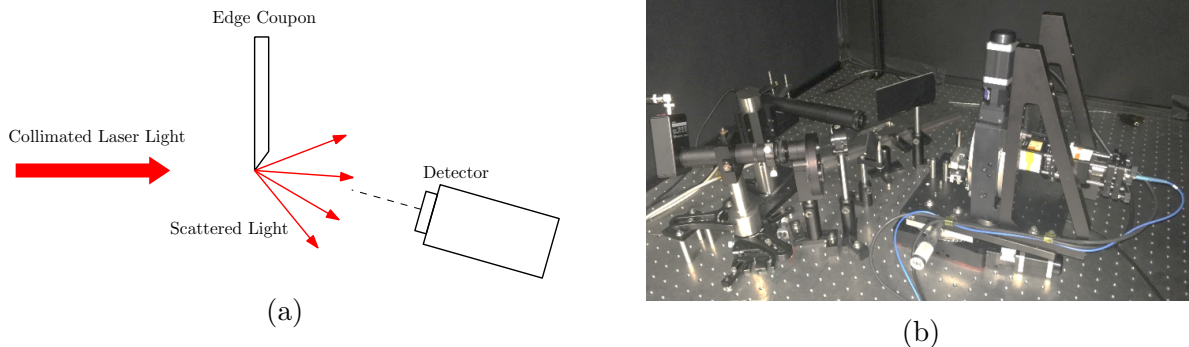

Figure 5: (a) Simplified schematic of the Multi-Angle Scatterometer and (b) image of assembled instrument

3.2 Single-Angle Scatterometer

The SAS measures scatter along the length of an entire edge up to 1 m long, but only over a fixed cone angle. Because the SAS has no means of measuring the unscattered beam, it has no absolute scatter calibration; it is used to determine the ratio of one scattering edge relative to another, *e.g.*, etched coupons relative to razor blades, and edge segments relative to coupons.

The optics of the instrument are composed of a 633 nm laser launcher, an alignment detector, and a camera tube. A test article is rigidly mounted while the instrument is fixed to two translation stages and one rotational stage, such that the camera can follow the edge and orient itself perpendicular to it. A final vertical stage is attached to the camera itself for focusing. Similarly to the MAS, a laser illuminates the terminal radius and scatters light into the camera. The camera images the scattered light, and the sum of pixel brightnesses is converted to a relevant scattered light measurement. A schematic of the major components as well as a picture of the device are shown in Figure 7. Example images taken with the camera are shown in Figure 8. All detectors and the camera have narrow bandpass filters to remove the majority of room light. More detail on each component and the operation of the instrument follows.

A laser beam enters the system horizontally through a single mode optical fiber and laser collimator which expands the beam into a roughly 10 mm diameter circle. The beam is linearly polarized such that equal power is measured in both S- and P- polarizations at the output. The polarized beam passes through a 10:90 (R:T) non-polarizing beamsplitter. The reflected light is then measured with a silicon detector to monitor power fluctuations. The majority of the light passes through and is reflected up toward the test article with a folding mirror, illuminating the terminal edge from below.
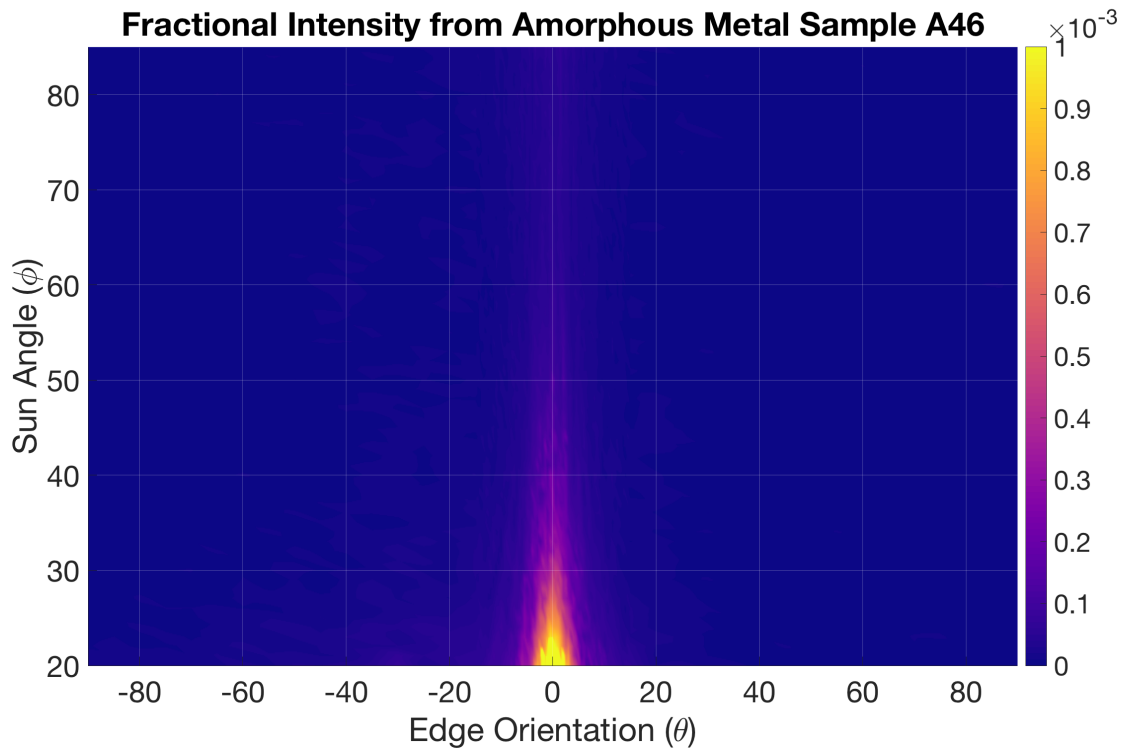
Figure 6: Fractional intensity heatmap from an amorphous metal sample, with sun orientation on the horizontal axis and angle to the starshade normal on the vertical axis.
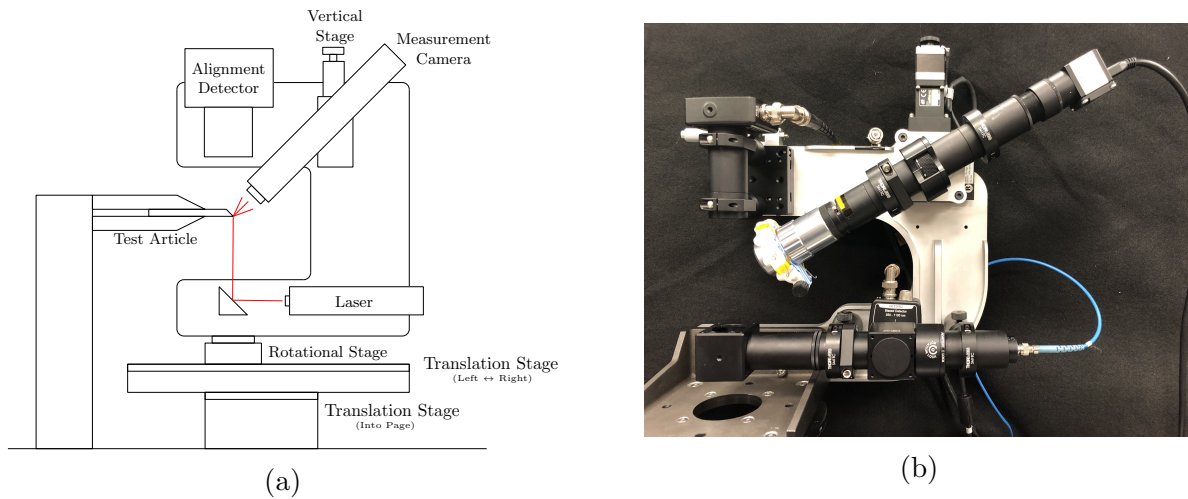

Figure 7: (a) Schematic diagram of Fixed Angle Scatterometer setup and (b) image of assembled instrument
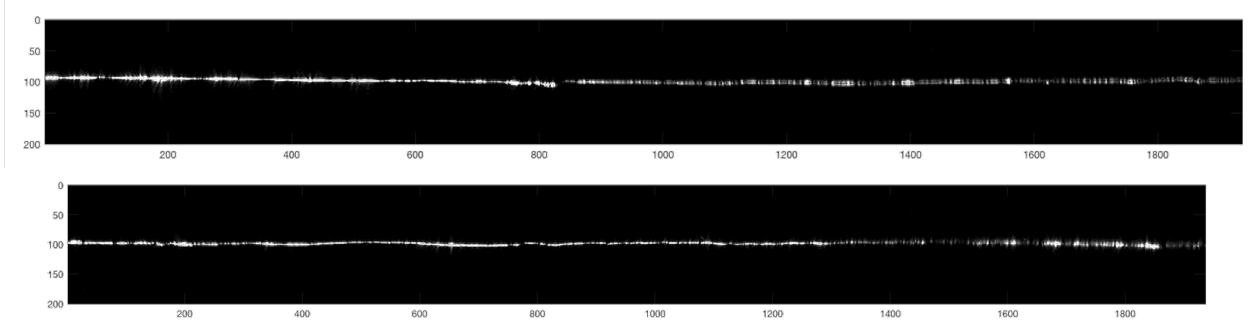
Figure 8: Two images of scattered light from an optical edge segment taken through the microscope objective. Axis units are in camera pixels. The field of view is approximately 1mm.

An alignment detector is positioned above the sample and consists of a collecting lens, an ND filter, a bandpass filter, and a silicon detector. The alignment detector monitors the position of the instrument relative to the terminal edge and is used to ensure that the laser is centered on the edge.

The camera tube consists of a long working distance 10x microscope objective with an acceptance angle of $\sim$30°, a focusing lens, linear polarizer, bandpass filter, and a high-resolution CMOS monochrome camera. The scattered light from the terminal edge enters the objective and is focused through the filters onto the camera. The camera is able to image roughly 1 mm of edge at a time. At each measurement location, light is gathered over a 1 mm length of edge at sun angles between 45° and 75° of normal.

The translational stages consist of a 1 m longitudinal stage, a perpendicular 200 mm stage for lateral movement, a rotation stage, and a small 15 mm vertical stage. The optics are held to the rotation stage with an aluminum bracket. The vertical stage is also mounted to this bracket and holds only the camera tube, as the other optics do not need a vertical range of motion.

The instrument is aligned to a test article by manually finding the corners of the terminal edge using a reticle on the camera output. Using this process, the instrument can be repeatably positioned within 50 μm. The position of the edge is then interpolated by the software using user defined parameters. As the SAS moves, it re-centers and refocuses itself on the terminal edge at each measurement location. At each measurement point, the instrument converts quantity of light collected by the camera to an effective brightness at the telescope.

A sample set of SAS output data is given in Figure 9. Each data point on the plot corresponds to a separate SAS measurement at 1 mm spacing along the edge. Each measurement is the integral of the light across the camera, examples of which are shown in Figure 8. The y axis units are the fractional scatter at a distance of 1 m, for a 1 m length of edge, at a wavelength of 633 nm. The scatter scales inversely with distance squared, and linearly with segment length. The diffraction component scales linearly with wavelength, and the reflection component scales with the material reflectivity properties.

The fractional intensity scale in Figure 9 was determined by comparing the SAS segment scatter to the mean SAS scatter from a set of coupons. The coupons were also measured on the MAS where their absolute scatter characteristics were determined. The process of

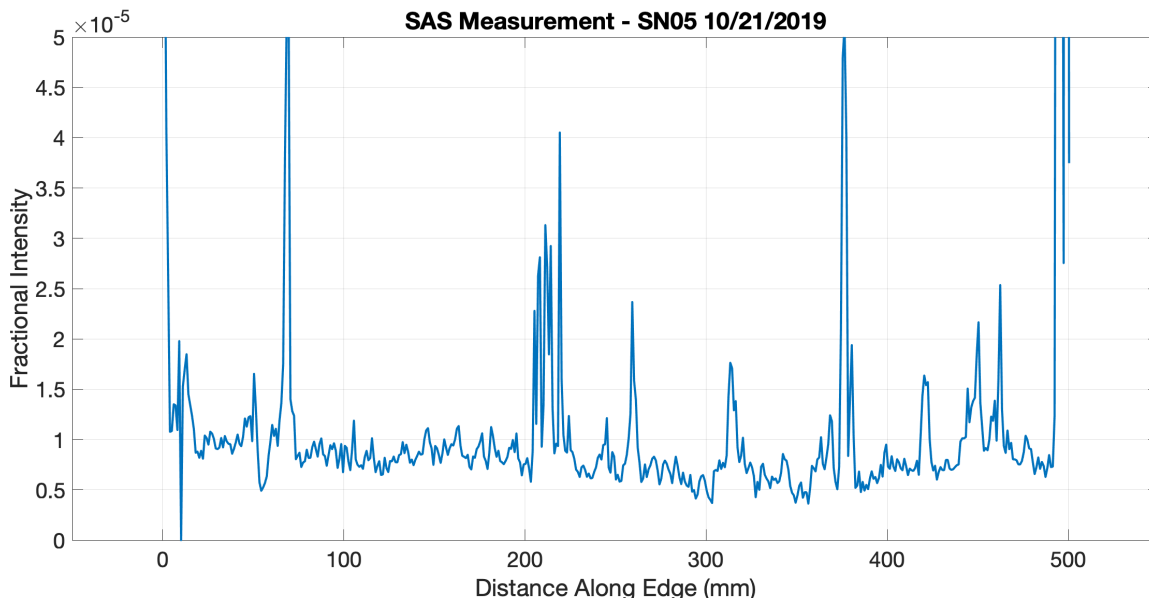linking the SAS and MAS measurements is described in the following section.

Figure 9: Sample data taken with the SAS instrument

To verify SAS repeatability, a single edge coupon was measured over the central 90% of its length on six separate occasions during the six week course of the milestone data collection. The resulting repeatability of the mean scatter had a standard deviation of 0.9%. In practice, reference coupons are measured regularly to ensure that the instrument is not drifting.

3.3   Relating the SAS to the MAS

The pattern of solar glint lobes on the starshade shown in Figure 2 is computed from the local (θ, ϕ) values of the MAS coupon heat map (Figure 6). Edges oriented near the specular angle $\theta = 0°$ are bright; the glint lobes are concentrated in these regions of the starshade. The angle of an illuminated starshade petal edge can take on any value $-90 < \theta \leq 90$ (the other half is purposely blocked from direct solar illumination by the geometry of the edge structure). Part of this range $(-45 < \theta \leq 45)$ is represented on the horizontal axes of Figure 10 and by the rectangle spanning the width of the MAS heatmap.

The MAS measures only optical edge coupons while the SAS measures both the coupons and the optical edge segment assemblies, but only over a subset of the MAS range of angles, albeit at the angles most relevant to the operational range of the starshade. The SAS acceptance cone is represented by a circle with a 15° radius overlaid onto the heatmap as shown in the right side of Figure 10. The SAS measures the integrated scatter within the circle; it does not return the local scatter information separating the specular and diffuse components.

For a given coupon edge, the ratio of the light within the SAS acceptance cone to the light within the full MAS rectangle is termed the selection ratio, ρ. A perfectly specular
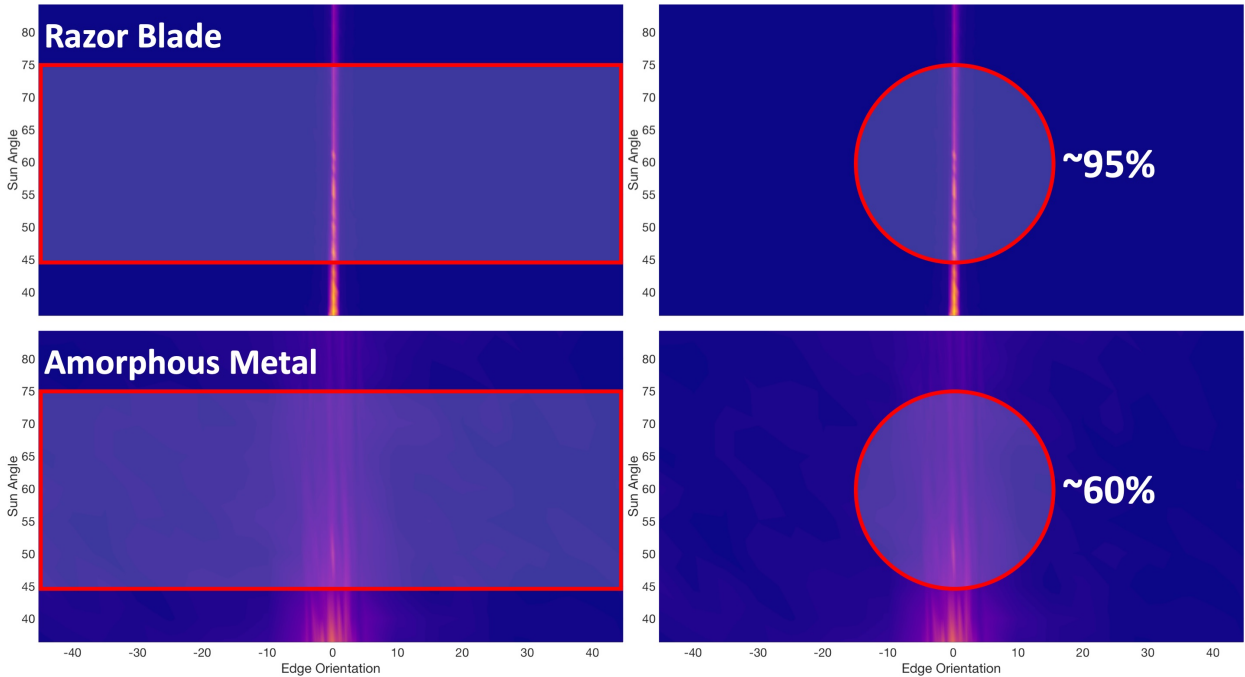
Figure 10: Heat map plots indicating the difference between a new, highly specular razor blade and a more diffuse amorphous metal edge between the two scatterometer testbeds. The circle represents the SAS acceptance cone.

edge will only reflect light at $\theta = 0°$, leading to a selection ratio of unity. Razor blades are highly specular reflectors and we find $\rho = 0.95$. Amorphous metal blades are more diffuse and the selection ratio drops to $\rho \approx 0.6$. Measurement data supporting this result will be discussed in Section 6.

The link between the SAS and the MAS is the circular region of the heatmap. This is the region of (ϕ, θ) space that is sampled by both instruments. In Section 6 we will show that there is good consistency in the value of ρ over a wide range of coupon scattering quality.

3.4 Optical Experiment and Glint Calculation Process

Now that we have introduced the nature of the glint from the starshade optical edges, the instrumentation used to measure edge scatter, and the link between the two instruments, we discuss the process of calculating the starshade glint from scatter measurements of optical edge segments. This process is depicted graphically in Figure 11. Later, in Section 7.1, we provide a detailed error budget for the glint calculation process.

First, edge segments and coupons are measured with the SAS. The ratio of the average scattered energies is the Segment to Coupon Scatter Ratio (SCSR). The same coupons are measured on the MAS, and from that an average heatmap is computed. It is then multiplied by the SCSR. The SISTER software reads in the scaled heatmap and computes the solar glint pattern.

The overall analysis flow, including comparison to analytical models, computation of
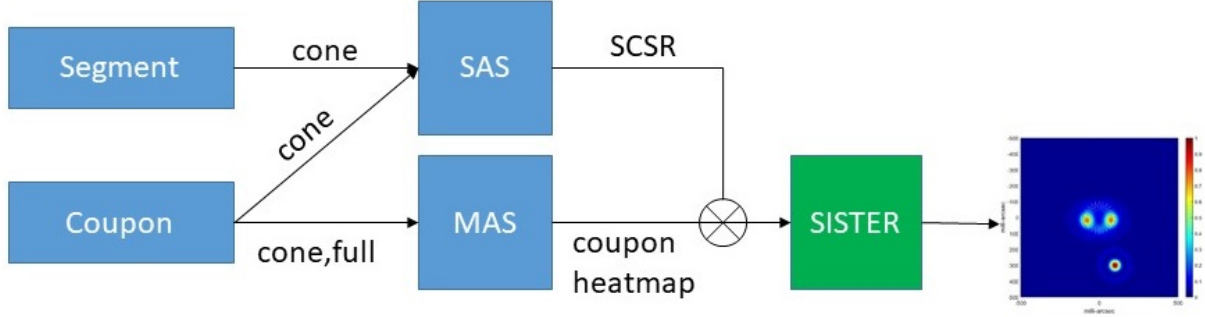
Figure 11: Flowchart of measurements and analysis. Solar glint is computed from the average coupon scatter heatmap multiplied by SCSR.

average heatmaps, and consistency checks between the instrument is shown in Figure 12. We start with 500 mm long optical edge segments, and 50 mm long optical edge coupons, as shown in Figure 4. The parts are measured before (when possible) and after environmental testing which was performed on all segments and a subset of coupons (coupons A14, A21, and A23). The SAS measures the scatter along the length of the segments and coupons, returning a single value, the relative amount of scatter, at each position. This value has an arbitrary, but stable instrument scale factor. The scale factor is of no consequence (if stable) because we will always compare the ratio of segment scatter to coupon scatter, the SCSR.

The MAS measures only coupons. A MAS measurement consists of the detection of scattered light at various source and edge orientations (ϕ, θ), relative to the detection of the source shining directly into the detector. The output product is a heatmap of the fractional scatter (Figures 6 and 10). The heatmap is scaled to represent the fractional scatter per meter of edge, at a distance of 1 m from the edge, taking into account the angular size of the sun.

Unlike the SAS, in the MAS, calibration of the ratio of scattered to direct beams is critical. Fortunately, most parameters of the MAS are common to both measurements, including beam power, aperture size, integration time, polarization state, and the detector. An intensity monitor is used to measure and calibrate the small ($\sim 1\%$) fluctuations of the beam power during the experiment. However, there is one significant difference between the scatter and direct measurements: a neutral density filter with OD$\sim$ 7.2 is used to attenuate the direct beam. Calibration errors of this filter directly scale the heatmap, and with it the predicted flux of the glint lobes. We have calibrated the filter, which actually consists of two cascaded filters with ND=2.5 and ND=4.7 filter, to a precision of 5% and cross-checked with two independent power meters.

We form an average heatmap from the set of coupons. We multiply the heatmap by the SCSR resulting in a scatter function whose amplitude is consistent with the segments, and whose angular dependence is measured on coupons. Plots of SAS coupon and segment data show that they behave similarly along their lengths. The resulting heatmap is read by SISTER which computes the glint pattern by identifying the angle relative to the sun and telescope of the locus of points forming the starshade edge. The angular components of the edge orientation correspond to the scatter ratio at a point in the heatmap. These are
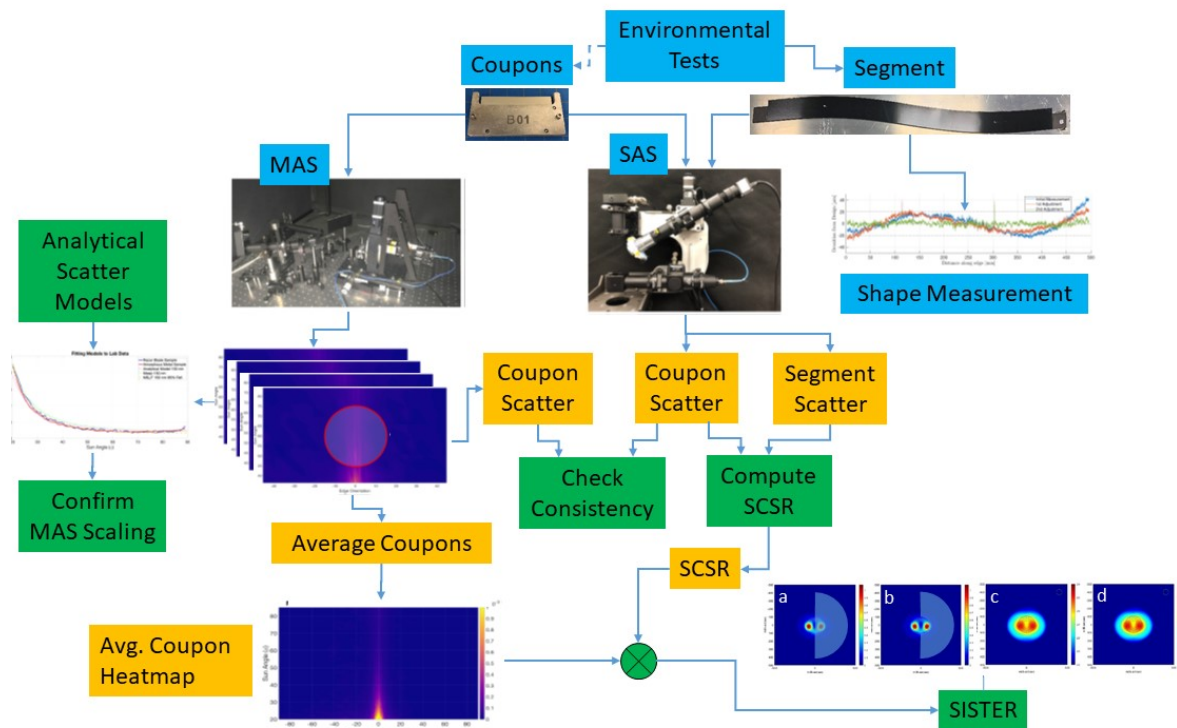
Figure 12: Overall experiment implementation. Orange boxes are data. Blue boxes are hardware. Green boxes are software and analysis tools.

identified and convolved with the telescope point spread function to form the image of the glint pattern.

Finally, we analyze the total equivalent magnitude of the glint lobes, the total energy outside the IWA, the brightest point outside the IWA, the average brightness at the IWA, and the fraction of pixels at the IWA that are fainter than V=25.

4   Optical Edge Mechanical Design

4.1   Design Overview

The optical edge precisely defines the perimeter of the starshade, and more specifically each petal. It is not continuous, but is made up of segments approximately one meter long that are bonded to the structural edge of the petal, as depicted in Figure 13. The structural edge is a continuous piece of CFRP defining the perimeter of the petal primary structure.

A cross section of an optical edge bonded to the petal is given in Figure 14a. The substrate CFRP layup matches that of the structural edge. It provides structural support to a 38 micron thin amorphous metal foil. The edge of the foil defines the terminal edge of the segment and therefore the petal. The components are bonded together with EA9394 epoxy, chosen for its relatively high strength across a broad and relevant temperature range, creep resistance, long pot life, and history of use in flight programs. Two bond operations
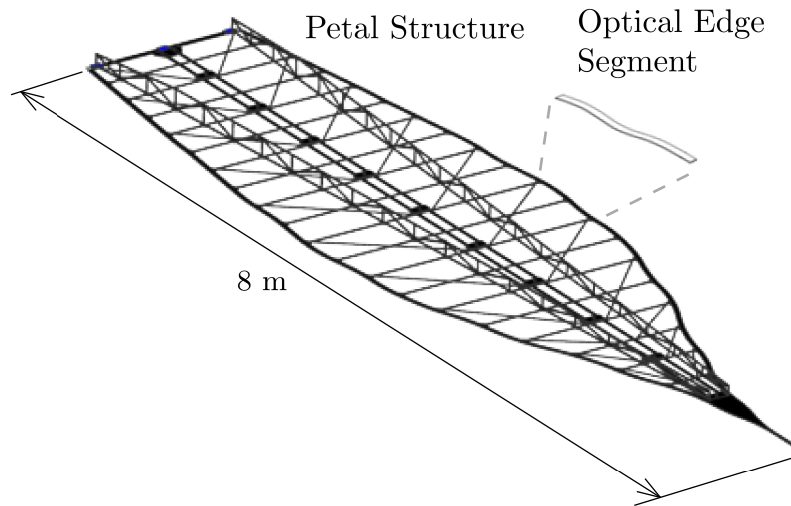
Figure 13: Petal mechanical structure with placement of optical edge shown.

are necessary to assemble an optical edge: first the amorphous metal is bonded to the CFRP substrate to produce a segment, then that segment is bonded to the structural edge. The substrate is bonded to within 0.64 mm of the terminal edge to support the thin foil, while the structural edge is offset approximately 12 mm inboard to prevent sunlight from illuminating the telescope side of the starshade. All bond line thicknesses are controlled using 0.005" diameter glass beads. A detail of the terminal edge is provided in Figure 14b.
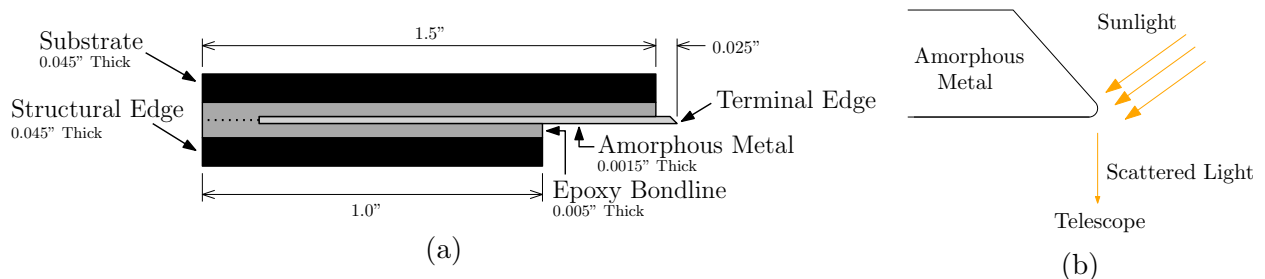

Figure 14: (a) Cross section of optical edge flight and prototype designs, see Section A-A in Figure 15 and (b) detail of terminal edge.

Amorphous metal is chosen to form the terminal edge due to the results of a previously performed trade study.[3] The grains in traditional metals create large, irregular etched feature sizes, resulting in more scattered light reaching the telescope. In contrast, the glassy molecular structure of amorphous metals results in a relatively smooth and thus sharp bevel well suited for this application. The specific alloy used is known by the trade name MBF23 and is manufactured by Metglas Inc. The alloy constituents include 60.5% Fe and 30% Ni by mass percent, along with small amounts of Cr, B, and Si. Previous work[6] also investigated applying commercial black coatings to the amorphous metal in an effort to reduce reflectivity, and therefore the scattered light. However, these coatings increased the terminal radius enough to cause a net increase in scattered light.

15

4.2   Test Articles

Two sets of test articles were fabricated: assembled 500 mm segments and standalone 50 mm amorphous metal coupons. The segments incorporate etched amorphous metal bonded between two pieces of carbon fiber as depicted in Figure 14a. The segments are too large to be measured in the MAS. Therefore, coupons manufactured in the same lot as the segments were used to characterize the performance of bare amorphous metal over all potential sun angles as well as to establish a calibration constant between the MAS and the SAS, as described in Section 3.3.

4.2.1   Segments

A total of six prototype segments were constructed as part of the MS3 effort. The segments are full scale in cross section, and at 500mm long, are approximately half scale in length as compared to the flight design. This section describes the design and manufacturing process for segments in detail.

4.2.1.1   Segment Design

The design of the segment test articles is derived directly from the flight design described in Section 4.1. The cross section is identical to that shown in Figure 14a, however the in-plane shape of the segment is a 500 mm long sinusoid with a peak-to-peak amplitude of 20 mm, as shown in Figure 15. This shape was chosen because it is consistent with the expected curvature of the petal and enables easy detection of in-plane shape changes with traditional data analysis tools. Although the length is about half that of full scale, all other dimensions (e.g. thickness and width) are full scale to preserve critical dimensions for manufacture and test. Additionally, all components are flight grade materials. The structural edge is included in the assembly and extends 25 mm beyond the ends of the substrate to mimic the continuous nature of the petal structure.
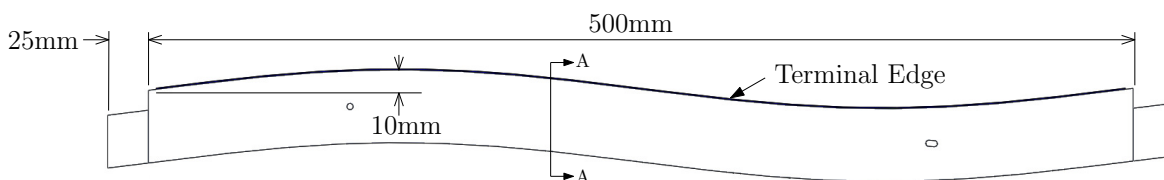
Figure 15: Layout of an as-built optical edge segment. The cross section A-A is given in Figure 14a.

The purpose of constructing these segments was to demonstrate scatter performance before and after environmental tests as defined in MS3, and separately to verify in-plane shape performance (see Appendix A). Note that the tip segments which are manufactured through the same process, as well as the integration of segments onto a petal, are addressed by Milestone 5b.

16

4.2.1.2   Segment Manufacturing

Construction of the optical edge segments is a multi-step process. The amorphous metal was etched using a commercial process to form the precision edge while the CFRP structural components were routed from fabricated panels. The edge components were then bonded together with a multiple step bonding process to ensure the in-plane shape of the foil was preserved and the terminal edge not damaged.

4.2.1.2.1   Etching The amorphous metal parts were photochemically etched from a 190 mm wide sheet of raw material. The cutout pattern is shown in Figure 16. Note a sinusoidal slot that defines the terminal edge, a hole and slot that engage tooling pins during bonding, and a pattern of large holes used for mounting the sheet during transportation from the vendor. More material than is needed to form the edge was designed into each sheet due to a concern that the amorphous metal would distort prior to bonding without sufficient support material. However, this was found not to be an issue, so the excess material was removed with shears before bonding and has since been removed from the design.
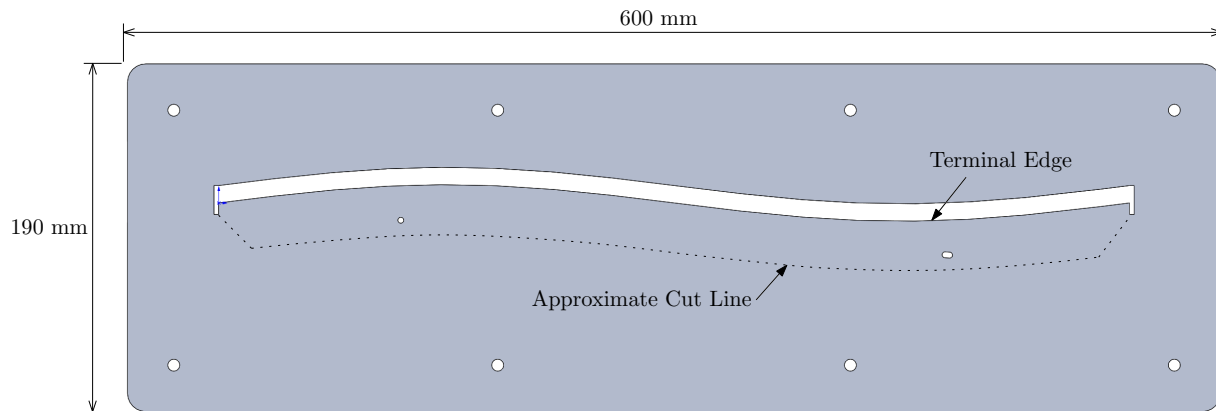

Figure 16: Etch pattern for the amorphous metal sheet. Also shown is the approximate location where the amorphous metal was sheared from the sheet.

4.2.1.2.2   Bond Preparation To promote adhesion, the amorphous metal surface was cleaned first using acetone and then ethanol wipes. No other surface preparation was performed. Abrasion was previously attempted on test samples but caused the thin foil to deform out of plane and risks damaging the terminal radius, and therefore was not implemented in these test articles. After cleaning, the amorphous metal was secured to a custom vacuum table for bonding.

The vacuum table was used to restrain the foil and maintain in-plane shape tolerances during bonding. The table features 0.25 mm diameter micro-holes spaced 4.75 mm apart in a pattern that matches the curve of the edge. It incorporates two alignment pins that engage a hole and slot in the prototype hardware. To preserve optical properties, the table incorporates a cutout that matches the shape of the terminal edge ensuring the edge does not contact the tooling. For bonding, the table was masked with a 0.003" thick Teflon sheet

to prevent inadvertent adhesion of the AM to the vacuum table. Holes were poked in the Teflon over all necessary vacuum holes. The alignment pins were coated with a thin layer of bond release to prevent adhesion of the pin to the edge. An amorphous metal component secured to the vacuum table is shown in Figure 17a.

The bonding surfaces of the CFRP were cleaned with isopropyl alcohol (IPA), abraded with ultra-fine 7447 Scotch-Brite, and cleaned again with IPA until no residue remained. Care was taken to not break any fibers and to ensure abrasion was evenly applied. Bonding was completed within four hours of all surface preparation steps.

4.2.1.2.3   Bond Operations The first of two bond operations was to adhere the amorphous metal to the CFRP substrate. This step only occurred after all surface prep was complete and the amorphous metal was secured to the vacuum table. Epoxy was applied to the CFRP using a screeding process. Two rails matching the shape of the substrate were shimmed to be a known height above the component. After epoxy was initially deposited onto this surface, a flat bar was run across the rails such that a controlled thickness of epoxy was left on the carbon fiber. The desired bond line thickness was 0.005," so 0.008" of epoxy was screeded onto the carbon fiber to ensure that there was enough to account for variability and produce some squeeze out. Glass beads were used to control the bondline thickness and were added to the epoxy while mixing. The screeding step was completed on a second vacuum table to secure the substrate.

Before moving on, the thickness of the epoxy layer was verified with a wet film thickness gauge. Typically, a thickness within 0.001" of the desired value was achieved. If not, adjustments could be made and the process repeated. After an acceptable thickness was achieved, an additional screed was done to remove the gauge indicator markings in the epoxy. Figure 17b shows an edge in the screeding fixture after epoxy application. The carbon fiber was then removed from the table and the perimeter cleaned of excess epoxy.

The substrate with epoxy was then placed face down on top of the amorphous metal, and a pressure of 4 psi applied using weights. The load was distributed using 19 mm thick aluminum bars with a thin layer of rubber for compliance, and stabilized using tubing placed perpendicular to the edge. Figure 17c shows the loading fixture in use. By design, epoxy squeezed out of the joint until the assembly rested on the glass beads. Excess epoxy was cleaned up with Q-tips.

The second bonding operation involved adhering the structural edge to the substrate/AM assembly. In a flight case, the structural edge would be part of the petal and the substrate/amorphous metal assembly bonded to it. However, for this prototype build, the substrate/amorphous metal assembly was placed on a flat plate with the amorphous metal facing up. The plate had two pins which engaged the alignment features. Epoxy was screeded onto the structural edge, the structural edge placed on top of the substrate/amorphous metal assembly, 4 psi of pressure applied, and squeeze out cleaned up much in the same way as described in the previous paragraphs. The load was removed after 24 hrs, and the completed optical edge assembly left to fully cure for five days per the manufacturer cure schedule.

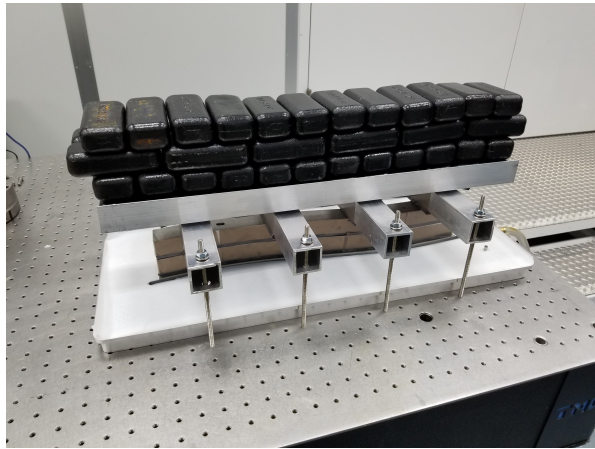Figure 17d shows the front and back sides of two of the completed edges. Optical performance of the segments is discussed in Section 6.
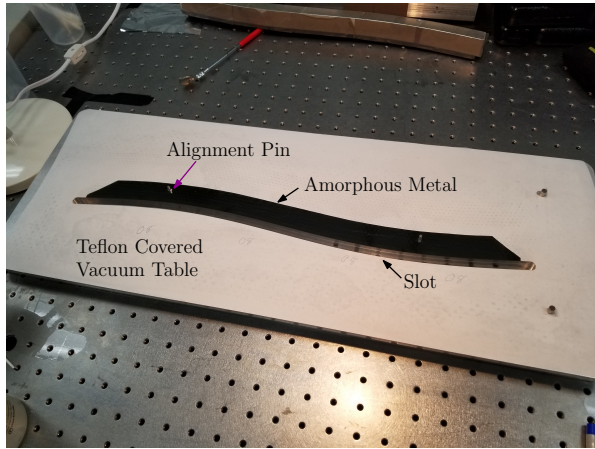
(a)

(b)

(c)

(d)

Figure 17: The assembly process includes (a) placement of the amorphous metal onto a vacuum table, (b) screeding fixture with epoxy applied to a component, (c) application of pressure to a bond line and (d) the top and bottom sides of two completed optical edge segments.

4.2.2 Coupons

The coupons were etched in the same lot as the segment amorphous metal and are 25 mm wide x 50 mm long rectangles with straight edges (i.e. they do not have the curvature of the petal). Since the coupons were etched at the same time as the segments, they have the same precise beveled edge and sharp terminal radius. Importantly they are small enough to be measured by the MAS. The performance of the coupons was checked before assembly of the segments to establish confidence that the segments would meet scatter requirements. Special handling processes were established to ensure that the terminal edge was not damaged before testing. Each coupon was placed in a two-part aluminum container that protected the terminal edge, but also allowed for scatter testing and SEM imaging. An image of a coupon in its aluminum holder is shown in Figure 18. Note that the coupon is simply clamped in the holder and not held with epoxy. These coupons are of the same design previously used in trade studies to test variables in the manufacturing process and coatings.
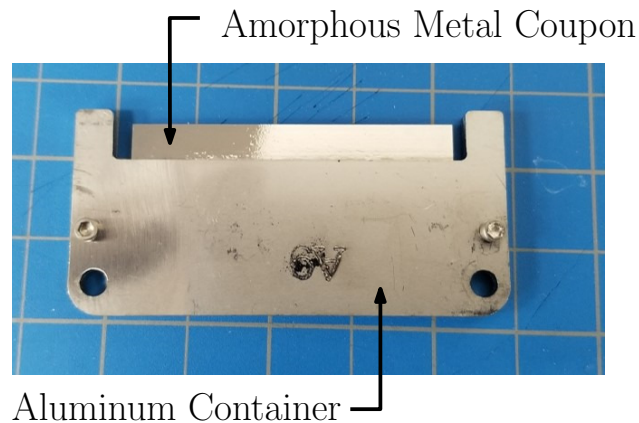

Figure 18: Image of an amorphous metal coupon mounted in a custom aluminum bracket for protection.

5 Experiment

The scattered light performance of the segments was characterized before and after "relevant thermal and deploy cycles," per the MS3 definition. This section describes the tests performed to meet the milestone along with thermal models used to determine the expected flight temperatures and actual prototype test temperatures and sequences. Performance results are discussed in Section 6.

5.1 Relevant Tests

The relevant criterion in defining the stressing environments for the optical edge was whether or not the environment could have a detrimental effect on the scatter performance of the terminal edge. In other words, the most critical environments are those that could change the physical attributes of the sharp terminal edge which scatters sunlight. Two environmental

tests were deemed to fit this criterion: (1) stow and release cycles at ambient temperature and pressure and (2) thermal cycles in the deployed configuration.

Stow and release cycles will be performed at various points throughout a flight test campaign. Although the strain in the amorphous metal will be small due to its proximity to the neutral axis, there is an unknown and difficult-to-model potential for the furling strain to manifest itself as physical change of the very thin and sharp terminal edge. This test captures the actual furling strain environment that the edges will see during the flight test campaign, and therefore any any change in scatter performance as well.

Thermal cycling in the deployed configuration serves two purposes. First, it will demonstrate whether or not exposure to the expected flight temperature extremes could result in sub micron level changes to the very thin and sharp terminal edge of the amorphous metal that affect scattered light performance. Second, because the AM is bonded to low coefficient of thermal expansion (CTE) CFRP, there is thermal strain between the AM and CFRP that could manifest itself in small mechanical perturbations of the terminal edge (i.e. micro-buckling); this test will demonstrate the extent to which the thermal strain affects solar scatter performance.

Stowed thermal cycles are important for determining the mechanical limits of the bond between the amorphous metal and CFRP structure in the space environment; therefore, thermal cycling in the stowed configuration was performed on edge assemblies at various temperature limits. Scatter performance was measured after the stowed thermal cycle environment to confirm the milestone assumption that it was not a stressing environment. A summary of the stowed thermal cycle testing is provided in Appendix B and the test history for each segment is in Appendix C.

An explanation of the stow and release cycles and deployed thermal environment follows.

5.1.1 Stow and Deploy Cycles

To stow a starshade, each petal is wrapped in a spiral pattern around the 2.25m diameter folded perimeter truss, although the spirally wrapped petal takes a slightly larger curvature. To conservatively bound the worst bending case, the test articles were stowed to a 2.25 m diameter. Although a starshade is only deployed once in space, the flight system is expected to go through a series of on the ground test deployments. For the purposes of this study, 10 cycles was determined to encompass the likely number of ground deployments a petal would experience.

The desired radius of curvature was achieved with a fixed displacement four-point bending fixture. The design of the fixture was driven by the desire to use the same fixture for stowed thermal testing, requiring it to fit inside an oven and to be easily transportable. The fixture was assembled using T-slotted aluminum framing and other off the shelf components. The top half of the fixture was constrained on two 19 mm diameter bushings. Displacement, and therefore curvature, was set by using three fine pitched 1/4-80 set screws on the ends of the fixture. The displacement-driven configuration is more representative of the boundary conditions of the flight hardware system and is more deterministic than a load driven configuration. This in turn improves the overall ability to correlate our test configuration to the our model.

The inner pins were set to be a distance of $L/4$ from the outer pins, where L is the

distance between the two outer pins. This configuration was chosen because it provides a sufficiently long region (250 mm) in the middle of the test article where theoretically constant curvature and zero shear are applied, while also avoiding excessive shear in the outer regions as compared to the expected flight values. A schematic and image of the bending fixture are shown in Figure 19.
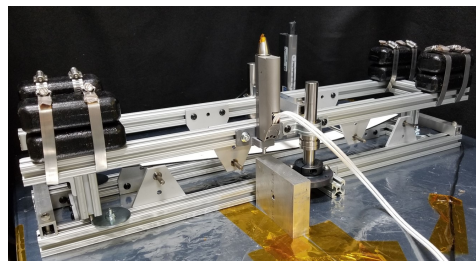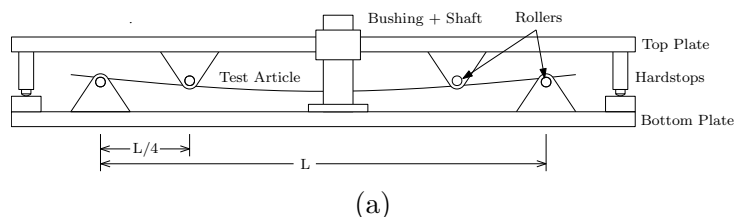

(a)

(b)

Figure 19: (a) Schematic diagram of the four point bending fixture and (b) fixture in use including loading weights, micrometers, and an installed edge (white)

The vertical displacement was set to achieve the desired radius of curvature of 1.125 m. Simple textbook equations and estimated bulk material properties were used to calculate the bending moment and shear in the test specimens under four-point bending,

$$M_{max} = F \cdot x \qquad V_{max} = F, \tag{1}$$

where F is the load applied to each pin and $x = \frac{L}{4}$. This estimation showed that the test articles should experience a bending moment of about 33.7 in·lbs between the two inner pins, and a shear load of 7.3 lbs in the outer regions. To verify that these loads are similar to what would be seen in a flight system, a petal-level finite element model of the stowed configuration, depicted in Figure 20, was analyzed. Shear and moment loads were checked throughout the deployment sequence in addition to the fully stowed state. The model showed a maximum shear load of 2.5 lbs and maximum bending moment of 31.5 in·lb in the optical edge, the maximum value being defined as the maximum average stress across the cross section of the edge. The test article conditions are considered to be representative and conservative for the flight petal.

After a test article was placed in the fixture, the raising and lowering rate was controlled with two motorized micrometers operating in tandem and programmed to move at a velocity of 0.5 mm/s, a sufficiently slow rate to simulate expected ground handling and flight deployment speeds.

Importantly, the starshade petals can be bent in one of two orientations depending on where they are attached on the truss. Since the neutral axis of the optical edge assembly is slightly offset to the substrate side, the metal foil can be put into either compression or tension depending on the bending direction. Therefore, half of the assemblies were tested with the amorphous metal in compression, and the other half in tension.
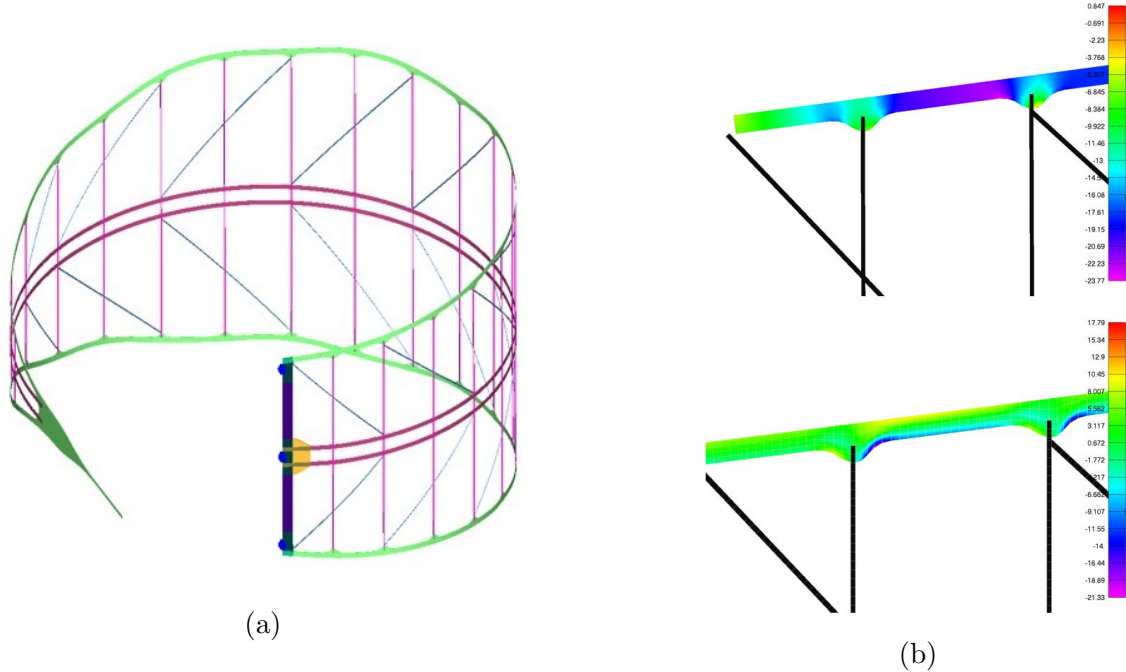
Figure 20: (a) Image of the fully stowed FEA model (colors coordinate with separate components) and (b) load distribution on the segments with maximum bending moment and maximum shear.

5.1.2 Deployed Thermal Cycle

The stressing condition for an optical edge in the deployed configuration is thermal loading resulting from the mismatch in CTE between the amorphous metal and CFRP components. The CFRP has a near-zero CTE while the amorphous metal has a measured value of 8.4 ppm/°C.

Deployed thermal cycling occurred in a nitrogen purged chamber at JPL. The edges were placed on a flat plate in an unconstrained state. A starshade system level thermal analysis was used to determine test temperatures. The FEM is detailed and incorporates all major components of the starshade including petal structure, optical shield, and other blanketing. It assumes all CFRP surfaces, except the optical edges, are covered in single layer insulation on the sun side, and a 3-layer optical shield on the telescope side. The sun-facing layer consists of a single layer of Kapton, doped with silicon on the sun side, and aluminized on the anti-sun side for favorable thermal properties. The two remaining layers are composed of Black Kapton XC for its low light transmissivity property.

The analysis assumed that the starshade would spin at 1/3 RPM. Because the spinning of the starshade equalizes the temperature of all like components on the starshade, the primary variable in determining the maximum and minimum temperature of the optical edge is the angle of the sun relative to the starshade. During science operations, the sun will fall between approximately 40° and 83° relative to starshade normal. In addition, the starshade must also be able to survive a sun angle of 0° as the starshade re-orients and maneuvers into position at next target star.

The maximum temperature of 80°C occurred when the sun is perpendicular to the starshade, sun angle of 0°, (Figure 21, note that only two petals are shown, and non-edge related petal components are hidden for clarity). The minimum temperature of -96°C occurred at a sun angle of 83° (Figure 22). The final test temperatures were +105°C to -125°C. This provided 25°C margin on the hot side, and 29°C on the cold side. As a general reference, JPL flight hardware qualification programs require 20°C margin on the worst case hot and 15°C margin on worst case cold. Note that a sun angle of 180° (sun shining on the telescope side of the starshade), while not a mission design case, was also analyzed and found to have nearly identical results to the 0° case.

The number of thermal cycles in the deployed configuration for the Starshade Rendezvous Mission (SRM), the reference mission for the S5 technology development, is estimated to be under 40. This is based on the number of target star re-orientations, a maneuver which results in the starshade changing orientation with respect to the sun, and thus cycling the temperature of the starshade. For this test a minimum of 25 cycles was performed on all edges, and 50 cycles on one edge assembly, as well as on the edge coupons.
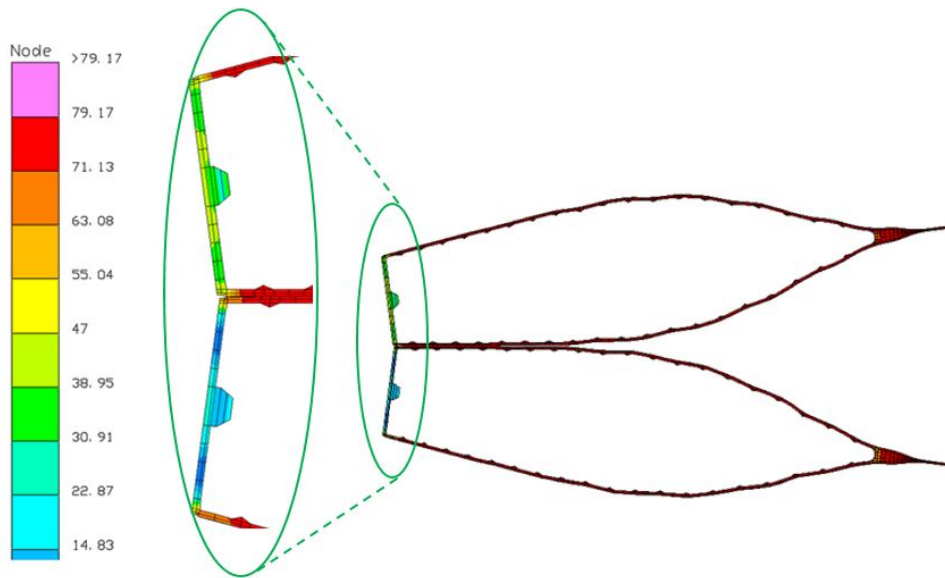

Figure 21: Detail of starshade model showing maximum temperatures along the optical edge of 80°C when sun is perpendicular to the starshade. Only two petals are shown and petal details are omitted for clarity.
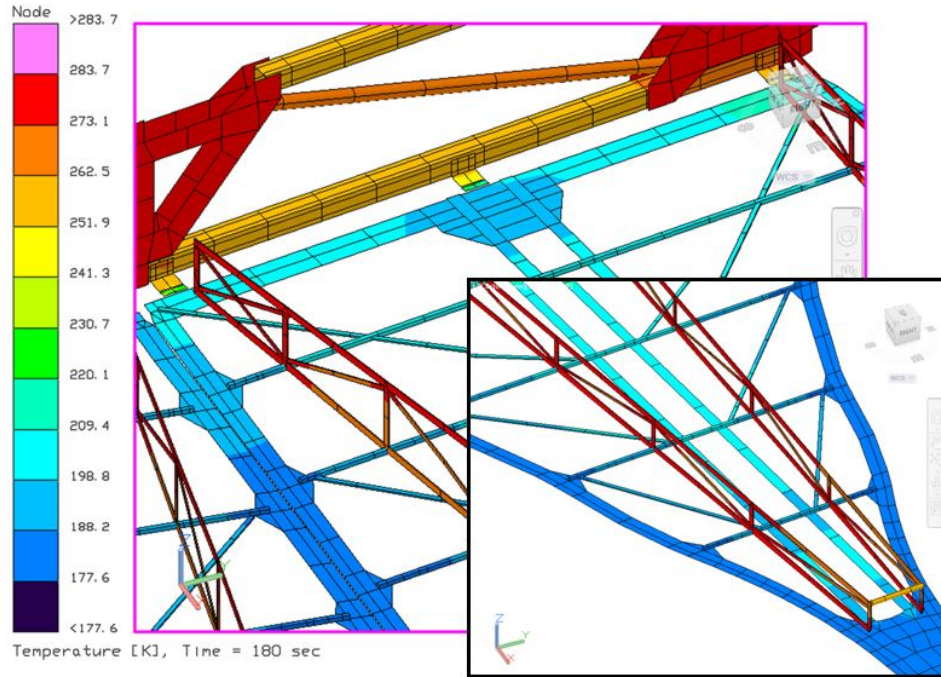
Figure 22: Detail of starshade model showing minimum temperature of -96°C when the sun is at at angle of 83°.

5.2 Test History

Of the six prototype segments that were assembled, four of the segments went through the complete set of environmental tests. Table 2 tabulates test history for each of these four segments and includes number of cycles for each test, whether the segment was bent into a direction that put the amorphous metal in compression or tension, and test temperature. The table includes tests considered directly relevant for MS3, however, each edge went through various additional test cycles during development. A full accounting of test conditions for each of the six segments is given in Appendix C.

Information is also provided for three amorphous metal coupons that went through thermal cycling. The coupons were not tested in bending due to their short length and because they were not mounted to CFRP, making the bending fixture impractical.

6 Test Results

6.1 MAS and SAS Coupon Scatter Measurements

A set of 13 coupons were measured on both the MAS and SAS (Table 3). Measurement dates indicate the MAS measurement. SAS measurements are all between October 18-22, 2019. The values in the "MAS cone" and "MAS full" columns are 10^6 times the average fractional energy over the cone and rectangle, respectively, per meter of edge, at a distance of 1 m from the edge. MAS measurements are correlated with the date, corresponding to

Table 2: Listing of relevant test history for test articles that completed relevant environmental tests.

	Bend and Release		Deployed Thermal Cycles	
	# Cycles	Bend Direction	# Cycles	Temperature (C)
SN05	10	Tension	25	
SN06	10	Compression	50	
SN07	10	Compression	25	+105/-125
SN08	10	Tension	25	
Coupons	N/A	N/A	50	

the 10% drift (1-sigma) observed with calibration coupons. The next column, MAS ρ, the selection ratio, is the ratio of the cone and full columns. Figure 23a shows that the selection ratio is uncorrelated with the level of coupon scatter. The mean value of ρ is the average fraction of the full scatter function that is captured in the 30° cone. The error on this value (Standard Error of the Mean (SEM) = 4.8%) represents the limitation on our ability to map the cone into the full scatter function. We use the SEM because the observed starshade solar glint pattern has contributions from many edge segments spanning tens of meters, thus the mean behavior of many edges will be observed. The spread of ρ values is smaller than the spread of MAS full and cone measurements, indicating that the selection ratio is largely independent of both the scatter properties of the edges and the long-term drifts of the MAS.

Table 3: Selection ratio for amorphous metal edge coupons

Coupon	MAS full	MAS cone	MAS ρ	SAS	MAS cone / SAS
A14 10/07/2019	6.8	4.6	0.67	4.3	1.05
A21 10/07/2019	7.3	5.0	0.68	4.6	1.08
A23 10/07/2019	8.8	5.2	0.60	4.8	1.09
A26 10/18/2019	7.3	3.1	0.42	3.6	0.86
A58 04/29/2019	8.4	4.7	0.56	3.9	1.19
B02 05/08/2019	6.6	4.1	0.62	3.4	1.20
B03 10/18/2019	5.5	2.6	0.48	3.0	0.87
B27 10/22/2019	4.9	3.4	0.69	3.6	0.92
B28 10/19/2019	3.6	1.6	0.45	2.1	0.77
B29 10/19/2019	4.6	3.1	0.66	3.4	0.90
B30 08/08/2019	4.1	2.4	0.57	2.5	0.95
B31 08/07/2019	5.3	3.8	0.71	3.9	0.96
B32 08/07/2019	6.0	4.2	0.70	4.3	0.98
MEAN±SEM	6.08±0.46	3.66±0.31	0.60±0.03	3.66±0.23	0.98±0.04
FRAC	**7.6%**	8.6%	**4.8%**	6.3%	**3.8%**

The table has a column of SAS coupon measurements as well. The SAS measured the same region of the coupon (3 mm wide, in three adjacent 1 mm measurements) as the MAS. Since the SAS has no absolute calibration, the measurements have been normalized to equal the mean of the MAS cone measurements. The MAS cone and SAS measurements are
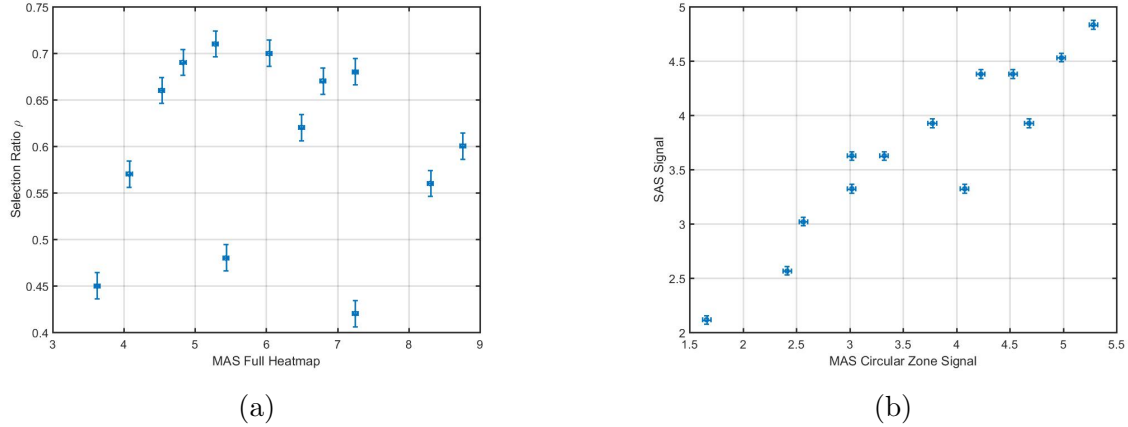
Figure 23: (a) MAS coupon selection ratio vs. integrated scatter (Scatter values are multiplied by 10^{-6}) (b) SAS integrated scatter vs MAS circular zone scatter. Error bars are estimated from short-term repeatability of the MAS and SAS measurements.

plotted in Figure 23b. If the SAS and MAS behaved identically, and if the MAS did not drift, then the last column, MAS cone / SAS would have values of unity. This is not the case, and we find that the SEM of the average ratio is 3.8%. This column is the key to linking the MAS and SAS measurements, and it shows that we can do so with a 1 sigma error of 3.8%. The inconsistency of the MAS Cone / SAS ratio is about half that of the MAS cone measurements. This is important because it indicates: 1) a significant part of the MAS full variations are not simply instrument drift; and, 2) differences between the two instruments are largely independent of the scatter properties of the edges.

6.2 Segment and Full Coupon Measurements

The main data product from the SAS is the SCSR. Table 4 lists the mean and median scatter measurements for the segments and the coupons, and the derived value of SCSR from the respective ratios. The segment measurements each represent the mean and median scatter over the central 400 mm of the 500 mm edge, after all environmental testing was completed. The last 50 mm on each end were measured (see Appendix D) but not included in the analysis due to thermal cycle-induced debonds between the amorphous metal and epoxy which complicated the alignment of the instrument. The coupon measurements represent the average of the coupons over their central 45 mm (out of 50 mm). Some of the corners suffered slight damage during separation and handling, so they were not measured. Mean results include all scattering sources over the analyzed regions, while the median is insensitive to the several peaks which may be due in part to assembly and handling issues. The median SCSR is 1.35, compared to 1.41 for the mean, demonstrating that the peaks contribute to only about 20% of the difference between segments and coupons.

Three of the segments, SN 6, 7, and 8, were measured in the SAS before environmental testing began. Table 5 shows the mean and median scatter values before and after environmental testing. *A key result of this study is that environental testing resulted in no significant change in scatter perfromance.* The before- and after- environmental testing scatter data is

shown in Appendix E.

Data for all of the coupons and segments appear in Appendix D. In the data plots there are a handful of locations where the data clearly spikes well above the mean. It is likely that these spikes can be attributed to particulate contamination or potential damage to the edge from epoxy removal. It possible that a very thin (e.g. 1 micron) layer of epoxy remains. This would be difficult to see in a microscope but would greatly increase the scatter compared to the 150 nm radius edge. If that is the case, then these spikes can be eliminated with better process controls in place.

We have also studied the potential contribution of the segment mounting to the overall scatter by comparing the mounted segments to unmounted segments (Appendix F). We found that the mounting may be contributing up to about half of the SCSR. Additionally, we looked for the possibility that the coupon mounts were contributing to the measured scatter (Appendix G). We found that at most the mounts contributed ~5% to the scatter. The measurement was limited by MAS repeatability.

We have highlighted in bold font the three error values in Table 3 that appear in the experiment error budget. They are:

- MAS full: this is the measure of the total energy scattered by the coupons. The mean value is our best estimate of the performance of coupons. The estimate is limited by our sample size to a fractional error of 7.6% (1 sigma).

- MAS ρ: this is the measure of the mean energy in the cone relative to the full energy, and is measured with a precision of 4.8%. The cone is the link between the SAS and the MAS.

- The MAS to SAS ratio (Column 6). This shows the variations between the two instruments when measuring the same part of the same coupon. The 3.8% error is the limitation on the precision of the SAS normalization. It can be improved with measurements of additional coupons.

7 Milestone Analysis

7.1 Error Budget

We estimate that the calculated glint lobe brightness is accurate to $\pm18\%$ 1-sigma. This is based on measurements of the instrument repeatability and accuracy, small sample size limitations of the coupons and segments, and the accuracy of the imaging code. These quantities are identified in Table 6. All values are listed in the table and in the discussion below are 1-sigma assuming a normal distribution.

7.1.1 Instruments

The MAS provides the heatmaps that are used to calculate the glint lobes. As noted in Section 3.1, the long-term (month-to-month) repeatability of the MAS heatmap level, based on measurements of a razor blade we use as a reference coupon, is 10%. The short term

Table 4: SAS Coupon and Segment Measurements

Coupon Name	Date	Mean Scatter	Median Scatter
A14	2019-10-22	6.2	6.0
A21	2019-10-22	6.9	6.3
A23	2019-10-22	7.2	7.0
A26	2019-10-21	5.4	5.2
A58	2019-10-18	6.0	5.9
B02	2019-10-21	5.1	5.1
B03	2019-10-18	9.0	5.6
B27	2019-10-22	5.6	5.7
B28	2019-10-22	3.8	3.8
B29	2019-10-22	5.1	5.1
B30	2019-10-22	4.3	4.0
B31	2019-10-22	7.3	6.5
B32	2019-10-22	6.9	6.8
MEAN±SEM (SEM%)		6.1±0.4(**6.7%**)	5.6±2.9(**5.1%**)
Segment Name			
SN05	2019-10-21	9.3	7.9
SN06	2019-10-07	8.8	6.9
SN07	2019-10-23	7.6	7.4
SN08	2019-10-23	8.4	8.1
MEAN±SEM (SEM%)		8.6±0.4 (**4.2%**)	7.6±0.3 (**3.7%**)
SCSR		1.41 ±0.11 (7.9%)	1.35 ±0.09 (6.3%)

Table 5: Segment scatter performance pre- and post-environmental testing

PRE-ENV. TESTING		
Segment Name	Mean	Median
SN06	7.7	6.7
SN07	8.8	8.5
SN08	9.1	8.7
POST-ENV. TESTING		
Segment Name	Mean	Median
SN06	8.8	6.9
SN07	7.6	7.4
SN08	8.4	8.1
RATIO (Post/Pre)	0.98 ± 0.15	0.94 ± 0.07

repeatability over the course of this experiment is much better (of order 2-3%) but ultimately the long-term stability limits our knowledge of the absolute scatter from the edges.

Table 6: Sources of Error in Estimating Solar Glint Lobe Brightness

Parameter	error (1-σ)	Notes
INSTRUMENT		
MAS repeatability	10 %	std. dev. of Instrument repeatability on a coupon (3 mm spot)
MAS scatter calibration	5 %	Knowledge of open beam ND filter OD
MAS length scale	2 %	Accuracy of distance from coupon edge to aperture (300 mm)
SAS Repeatability	0.9 %	std. dev. of instrument repeatability on a coupon (3 mm lengths)
COUPONS		
Mean coupon scatter (MAS)	7.6 %	SEM of coupon-to-coupon variability integrated over full range of angles
Mean coupon selection ratio ρ (MAS)	4.8 %	SEM of the ratio of coupon cone scatter to coupon full scatter
Mean coupon scatter (SAS)	6.7 %	SEM of coupon-to-coupon integrated scatter
Mean MAS to SAS ratio	3.8 %	SEM of relative cone scatter of same 3 mm spot measured on each instrument
SEGMENTS		
Mean segment scatter (SAS)	4.2%	SEM of segment-to-segment average scatter
ANALYSIS		
Imaging Code (SISTER) MUF	5 %	Consistency between analytical model and SISTER glint lobe
TOTAL		
Root Sum Square Error	17.6 %	Estimated 1 σ error on glint lobe brightness
Delta Mag 95% confidence	-0.28	1.65 σ

The MAS measures the ratio of the scatter at a range of angles to the unscattered beam shining directly into the detector. The optics, apertures, and detectors in these measurements are all common mode, except for a neutral density filter (actually a cascaded pair of ND filters) placed in the direct beam. An error in the measurement of the optical density of these filters directly translates to an error in the scatter ratio. We have measured the filters (OD=2.5 and OD = 4.68) and determined that the total optical density is 7.18. We measured the OD as a function of filter orientation (tilts, rotations, within reason for the experiment), and on two independent calibrated optical photometers. We found that the measurements repeated to a photometric precision of 5%.

The measured ratio is a function of the distance from the coupon edge to the detector.

Detection at longer distances will capture a smaller fraction of the light. The nominal distance in the MAS is 300 mm. With the defining detector aperture in a holder with a recessed edge, we conservatively estimate our distance measurement error is 3 mm (1%). The scatter ratio in the experiment depends on the distance squared; thus we report a 2% error on the length scale in Table 6.

The SAS reports a scatter value with an arbitrary (not absolute) scale. As noted in Section 3.2, the stability of the measurements over the course of the experiments was determined to be 0.9%.

7.1.2 Coupons

The manufacturing process produces coupons with varying scatter characteristics (Table 4). Our ability to measure the expected level of scatter and the selection ratio is limited by the finite set (13) of coupons. Here we report on the mean coupon behavior, and the standard error of the mean. This represents our limited ability to estimate the true mean level of scatter.

The MAS measures the scatter over the full range of solar angles and edge orientations. The mean value over the set of coupons has a standard error of the mean (SEM) of 7.6%. The MAS also allows us to measure the light within the angular cone sampled by the SAS. The measure of the cone on the MAS is what ties the MAS and SAS measurements together. The ratio of the MAS measured cone to the full angular measurements is what ties the cones to the expected on-sky performance. The MAS measured ratio between the light in the cone and the light over the full heat map (the 'selection ratio,' ρ) has a standard error of the mean of 4.8% (Table 3).

The SAS measures the coupons – this is the link between the MAS and the full length segments. From Table 4, the SEM of the mean coupon scatter measured on the SAS is 6.4%. Conservatively, we carry this error separately from the coupon variability observed in the MAS because at least part of the variability is due to the difference in the way that the instruments measure the scatter.

SAS coupon measurements are normalized to the mean of the MAS measurements. There are a number of reasons that the two instruments could measure different levels of scatter: they could be sampling slightly different regions along the edge; the central angle and diameter of the defining cone could be in error; and the SAS could apodize the received scatter (*e.g.*, field-dependent vignetting). The finite sample size of the coupon sample limits our ability to measure the sample normalization relative to the true normalization. The variability of this ratio (column 6 of Table 3) has an SEM of 3.8%.

7.1.3 Segments

We ran the full suite of environmental tests on four full segments (Table 4). While these segments had more widely varying scattering characteristics than the coupons, they were also 10 x longer, and their mean scatter had an SEM of 4.5%.

7.1.4 Analysis

The JPL-developed Starshade Imaging Simulation Toolkit for Exoplanet Reconnaissance (SISTER) is used to compute the solar glint lobes. SISTER reads the S- and P-polarization heatmaps generated by the MAS. It also reads in the locus of points constituting the outline of the starshade. Given the position of the sun relative to the starshade and telescope, it calculates the normals of the edges and determines where on the (θ, ϕ) heatmap to sample the scatter. The edges are categorized as 'leading' and 'trailing': leading edges are defined as having the sun-starshade-telescope angle less than $180°$. The light can reflect (and diffract) into the telescope. Trailing edges require the light to diffract toward the telescope, with no possibility of reflection. The code assumes that these edges are shadowed using the structure of the edge assembly (Figure 14a) and do not contribute to the glint. The code also assumes that the inner parts of the petal gaps, out to a radius of 7.5 m for the WFIRST Rendezvous starshade, are shadowed using small structures on the sun-facing side, and do not contribute to the glint. The contributions of all remaining edge segments convolved with the telescope point spread function at each wavelength being simulated.

To validate the accuracy of the SISTER calculations, we generated a test starshade with a triangular shape having a 1 m long edge oriented for specular reflection of sunlight. We assumed that the edge had a negligible terminal radius of curvature so that only diffraction was present. We applied the Sommerfeld diffraction equations for the 'S' (parallel) polarization and generated a heatmap for a specular edge. This heatmap was substituted for the experimental measurements. With the sun positioned at $\phi = 80°$ ($10°$ behind the plane of the starshade) SISTER then calculated a glint lobe.

We calibrated the magnitude of the glint lobe by modeling a planet of known magnitude. We used SISTER to generate a planet well to the side of the starshade (so as not to be attenuated by the starshade). We chose the host star to be the sun at a distance of 10 pc (V=4.83) and chose the planet to have a flux ratio of 8.55 x 10^{-9} (delta mag = 20.17). This created planet with a visual magnitude V=25. Comparing the planet the glint lobes, we found that the integrated light of the glint lobe was V=24.65.

We then compared this to the analytical calculation for a 1 m edge at the distance of the starshade (simply carried out on a spreadsheet), and assuming only that the Sun had a visual magnitude of -26.7, obtained the predicted glint result of V=24.70. We thus conclude that errors in the SISTER glint code are 0.05 mag, or 5%.

7.1.5 Final Experimental Accuracy

We assume that all of the aforementioned errors are independent and uncorrelated. Two of the parameters, the MAS and SAS mean coupon scatter, are partially correlated, but they are used independently to set limits on the instrument performance due to finite sized data sets, and the overall performance is only weakly sensitive to them (*e.g.*, removing the SAS mean coupon scatter would reduce our total error from 17.6% to 17% 1-σ).

Assuming a normal distribution, the 95% confidence level is 1.65σ, or 0.28 magnitudes. In the analysis to follow, we will report on the 95% confidence level by subtracting 0.28 magnitudes from the mean experimental result. Further refinement of this value will require 1) improved MAS stability, and 2) a larger sample size for both coupons and segments.

7.2 Magnitude of Solar Glint Lobes

7.2.1 Milestone 3 Compliance

The visual magnitude of the solar glint lobes is summarized in Tables 7, 8, and 9. The evaluation regions for the lobes are shown in Figure 24. The magnitude of the integrated light in a lobe (column 2 of the tables) is computed by integrating the glint over half the plane, as shown in Figure 24a. Much of this light is at radii smaller than the IWA. Column 3 is the magnitude of the integrated light at and beyond the IWA (Fig 24b) and is a full magnitude fainter. To identify a planet, a photometric aperture or matched filter would be used. In columns 4 and 5, and Figs. 24c and d, we have convolved the image with a photometric aperture whose diameter is equal to λ/D, with D=2.4 m for SRM and 4 m for HabEx, at the middle of each band (488.5 nm and 710 nm for the SRM shorter and longer bands, respectively, and 650 nm for HabEx). These images represent the signal that is measured in the photometric aperture at any point in the image plane. Column 4 and Fig. 24c are the magnitude of the brightest photometric pixel for radii $\geq$ IWA. Column 5 is the magnitude of the mean brightness calculated at the IWA along the path shown in Fig. 24d. This value represents the average signature of the glint lobes on the detection of planets at the IWA and is typically the value used in evaluations of starshade performance. In column 6, we include a MUF of 1.65σ by subtracting 0.28 magnitudes from the values in column 5 (see Table 6). The listed value is the 95% confidence level on the upper limit to the glint lobe brightness at the IWA. *We submit this column, highlighted in bold font, as the data supporting compliance with the milestone requirement for lobe brightness fainter than V=25.* Finally, in the last column, we show the fraction of photometric pixels at the IWA whose values are compliant with V>25 with 95% confidence. All pixels are compliant at the IWA for the WFIRST band 425-550 nm, and for HabEx as well. For the WFIRST band 615-100 nm, the fractional number of pixels fainter than V=25 ranges between 40% and 71%.
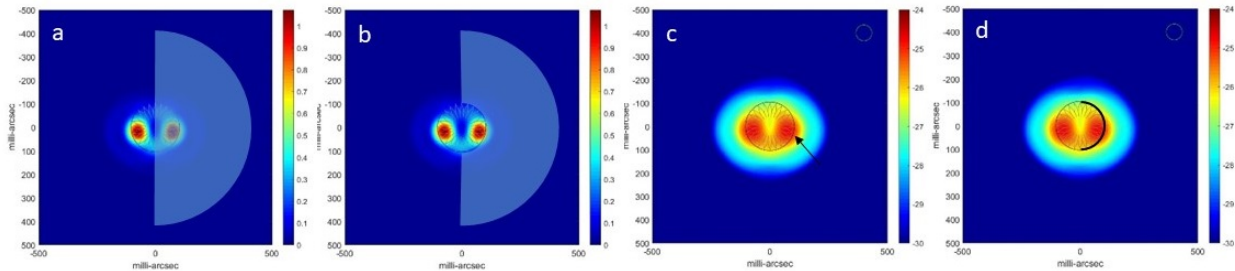

Figure 24: Evaluation of glint lobe magnitude.(a) The lobe magnitude is evaluated by integrating over half the plane. (b) The lobe magnitude is evaluated only for radii > IWA. (c) The image has been convolved to the resolution of λ/D. The brightest pixel at the IWA is evaluated. (d) In the same image as (c), the average value of the scatter at the IWA is evaluated.

We also show how the magnitude of the mean photometric pixel changes with working angle for the SRM (Figure 25). A vertical line marks the IWA radius: 72 mas for the 425-552 nm band, and 104 mas for the 615-820 nm band. The curves show that the glint effect diminishes with increasing distance from the starshade. At a distance of λ/D beyond the

Table 7: Estimated Glint Lobe Magnitude in WFIRST Rendezvous 425-552 nm Band

ϕ	Lobe mag[a]	r>IWA mag[b]	IWA Phot. min. mag[c]	IWA Phot. Avg. mag[d]	**IWA Phot. 95% conf.[e]**	IWA, V>25 Compliance
53	25.8	26.8	26.7	27.6	**27.3**	100%
63	25.9	26.9	26.9	27.7	**27.5**	100%
73	25.7	26.7	26.7	27.5	**27.3**	100%
83	25.2	26.2	26.2	27.0	**26.7**	100%

[a]Integrated magnitude of each lobe. See Figure 24 panel (a).
[b]Integrated magnitude of each lobe at angles > IWA. See Figure 24 panel (b).
[c]Brightest photometric pixel at the IWA. See Figure 24 panel (c).
[d]Magnitude corresponding to the average flux in photometric apertures at the IWA. See Figure 24 panel (d).
[e]Same as column (d) with the magnitude adjusted by -0.28 to account for experimental uncertainty (Table 6) at the 95% confidence contour.

Table 8: Estimated Glint Lobe Magnitude in WFIRST Rendezvous 615-800 nm Band

ϕ	Lobe mag	r>IWA mag	IWA Phot. min. mag	IWA Phot. Avg. mag	**IWA Phot. 95% conf.**	IWA, V>25 Compliance
53	23.7	24.7	24.6	25.5	**25.2**	67%
63	23.8	24.9	24.8	25.6	**25.4**	71%
73	23.6	24.7	24.6	25.4	**25.2**	64%
83	23.1	24.1	24.1	24.9	**24.6**	40%

Table 9: Estimated Glint Lobe Magnitude for HabEx 300-1000 nm band

ϕ	Lobe mag	r>IWA mag	IWA Phot. min. mag	IWA Phot. Avg. mag	**IWA Phot. 95% conf.**	IWA, V>25 Compliance
35	25.0	26.4	26.4	27.5	**27.2**	100%
45	25.6	27.0	27.1	28.1	**27.8**	100%
55	25.9	27.3	27.4	28.4	**28.1**	100%
65	26.0	27.4	27.5	28.4	**28.2**	100%
75	25.8	27.1	27.3	28.2	**27.9**	100%
85	25.2	26.6	26.7	27.6	**27.3**	100%

IWA of (112 mas in the 425-552 and, 166 mas in the 615-820 band), the average brightness has dropped by more than 2 magnitudes.
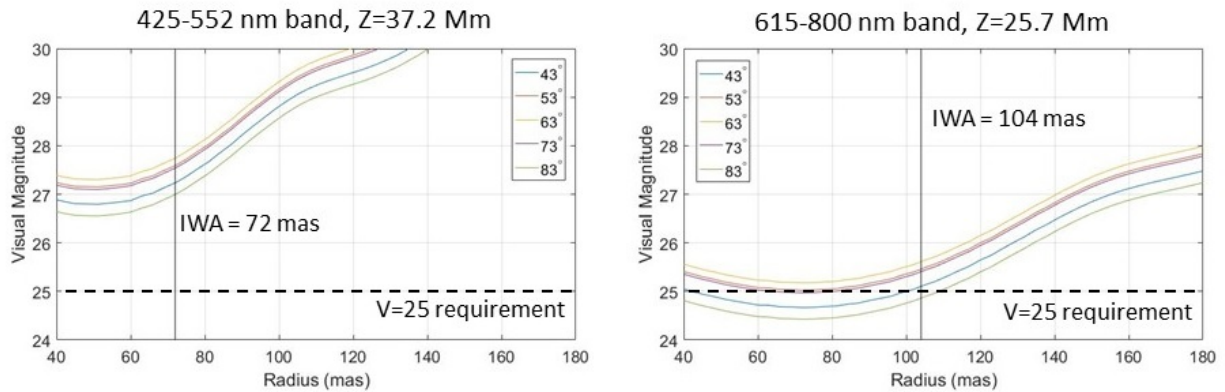

Figure 25: Magnitude of the WFIRST average level of illumination per lobe within a photometric aperture as described in Figures 2 and 24. Values at the IWA are in column 5 of Tables 7 and 8.

In summary, the results of Tables 7-9 show that at the 95% confidence level, over the range of wavelengths and angles relevant to WFIRST and HabEx, the average solar glint lobe effect at the IWA is no brighter than V=25 except at the extreme of solar angle in the 'green' band (615-800 nm). At that angle, 40% of the photometric pixels are fainter than V=25 after accounting for the 95% confidence uncertainty factor (0.28 magnitudes) These results are for the 500 mm long optical edge segments that scatter 41% more light (Δmag=0.37) on average than coupons, a result that is attributable to the assembly process.

7.2.2 Mission Performance Assessment

At the time of the Key Performance Parameter (KPP) and Milestone Reviews (July-August 2018), the milestone specification of solar glint lobes no brighter than V=25 was thought to be consistent with adding no more than 25% to the integration times driven by exozodiacal light. This is not the current assessment. The exozodiacal light level is currently specified at the median expected level of 4 zodis, or 20.5 mag arcsec^{-2}, where 1 zodi is 22 mags arcsec^{-2}. For the SRM band of 615-800 nm with a center wavelength of 708 nm and aperture of 2.4 m diameter, this translates to 26.84 mags per resolution element of $\pi(\lambda/D)^2/4$ area. Therefore, the specified solar glint is actually 1.84 mags or 5.5 times brighter than exozodiacal light, at the IWA and 1 AU solar equivalent distance from the star. This will significantly impact integration times for a planet appearing near the IWA. Solar glint rolls off with increasing angular distance from the starshade, as does the exozodi but at a slower rate. The SRM's focus on the closest stars, which gives ample habitable zone access, mitigates the impact to mission performance. This assessment will be reported in the future. Nonetheless, it is desired to significantly reduce solar glint.

Fortunately, there is much of room for improvement. In addition to the potential to produce segments that are close in performance to coupons, the bare metallic edges can be coated with a hybrid interferometric/absorptive coating presently under development. A

preliminary test in the SAS indicates a glint reduction by a factor of 14 over bare amorphous metal. Modeling with the Lumerical FDTD code verifies this factor (see Figure 3). This coating approach differs from our earlier attempts using relatively thick ($< 5~\mu$m) ultra-black commercial coatings that only increased the overall scatter,[6] presumably because of the greatly increased edge radius. The coatings also appeared to be fragile and were likely not compatible with many cleaning processes. The new design is a thin, robust, specular coating that reduces glint to levels well below even diffraction-limited razor blades. Further testing is underway, along with improvements to our instrumentation which lacks the sensitivity and wavelength diversity to fully test the parts. Additionally, a modeling effort is needed to understand how the coatings are reducing the diffraction component of the scatter. S5 is considering a plan to develop this coating along with improved testing and modeling capabilities with the possibility to repeat the OE segment tests presented herein for deploy and thermal cycles.

A second mitigating approach is to employ "stealth edges" which is a term we use to describe serrated edges placed where the specular reflection is greatest.[6] The serration removes the specular component for all but the tips and valleys of the edges and has been shown through MAS measurements to reduce scatter by up to an order of magnitude. The $\sim$ mm serration period has no effect on the starlight shadow. However, the stealth edges are not compatible with the baseline approach of spinning the starshade about its axis during an observation. This could lead to increased thermal deformation which in turn would degrade the starlight shadow. S5 is considering a trade study to determine if stealth edges with a non-spinning starshade are a superior solution.

8 Conclusion

This report details the S5 efforts to address Technology Milestone 3 regarding solar glint. It presents the optical edge design, custom scatterometer test equipment, relevant environments, the test plan, an analysis of error sources and an overall MUF, test results, and a path forward for improved performance. The demonstrated performance is fully milestone compliant at the 95% confidence level for the HabEx case and the SRM case at 425-552 nm. The SRM case at 615-800 nm is non-compliant over 60% of the IWA arc at the maximum sun angle of 83°. The results show that there was no degradation of performance due to thermal and deploy cycling.

Even at the milestone level, solar glint is the brightest source of background light and will significantly increase integration times for targets at the IWA. The mitigation plan here is to develop an improved edge segment bonding process of at least medium fidelity, and to explore the promising thin-film hybrid coating whose preliminary assessment indicated an order of magnitude reduction in glint. Because the coated edges show significantly less scatter than uncoated edges, it is imperative that we also improve the segment and coupon mounts so that they are not contributing to the measured signal.

References

[1] Willems, P., "Starshade to TRL5 (S5) Technology Development Plan," Technology Report, Jet Propulsion Laboratory (December 2018). https://exoplanets.nasa.gov/exep/technology/starshade/.

[2] Martin, S., Shaklan, S., Crawford, S., Lee, S.-C., Khayation, B., Hoppe, D., Cady, E., and Lisman, P. D., "Starshade optical edge modeling, requirements, and laboratory tests," in [*Techniques and Instrumentation for Detection of Exoplanets VI*], *Proc. of SPIE* **8864** (2013).

[3] Steeves, J., Martin, S., Webb, D., Lisman, D., and Shaklan, S., "Precision optical edges for a starshade external occulter," in [*Advances in Optical and Mechanical Technologies for Telescopes and Instrumentation II*], *Proc. of SPIE* **9912** (2016).

[4] Hildebrandt, S., Shaklan, S., Cady, E., and Turnbull, M. http://sister.caltech.edu (2019).

[5] McKeithen, D., Shaklan, S. B., Martin, S. R., Bradley, C., and Manthena, R., "Modeling the scatter of sunlight from starshade edges," in [*Techniques and Instrumentation for Detection of Exoplanets IX*], *Proc. of SPIE* **11117** (2019).

[6] Steeves, J., Lee, H. J., Hilgemann, E., Mckeithen, D., et al., "Development of low-scatter optical edges for starshades," in [*Advances in Optical and Mechanical Technologies for Telescopes and Instrumentation III*], *Proc. of SPIE* **10706** (2018).

[7] Hilgemann, E., McKeithen, D., Saltarelli, N., Ferguson, M., Steeves, J., Webb, D., Shaklan, S., Martin, S., and Lisman, D., "Advancements in precision edges for a starshade external occulter," *Proc. SPIE* **11117** (2019).

Appendix A: In-plane Shape Study

An individual edge segment must meet an in-plane shape requirement of ± 20 μm, over spatial scales >5 cm. The edge shape was characterized at various stages of the manufacturing and test process and the results showed that the segments meet this requirement as manufactured and after environmental testing.

A.1 Metrology System

A MicroVu Excel 1051 metrology system was utilized to measure the in-plane shape of the test articles. The machine pairs a precision x-y gantry system with a microscope head and edge finding algorithms. The measurement bed is 1050 mm x 1050 mm. An image of the system in use is given in Figure 26.
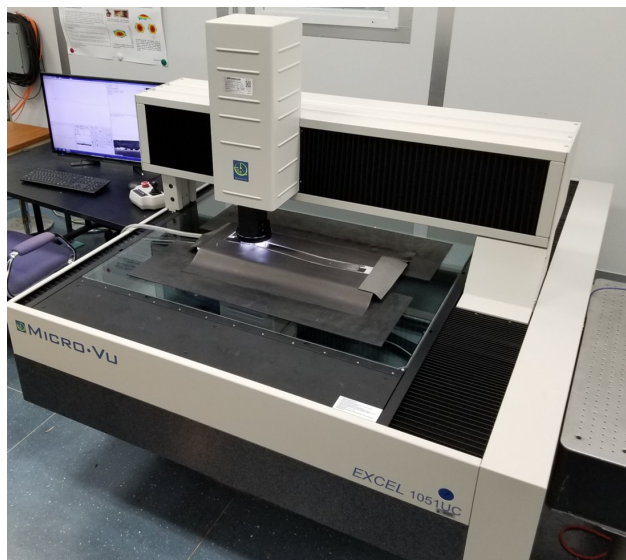
Figure 26: The MicroVu 1051 measurement system during measurement of an assembled edge segment.

The manufacturer specification of the machine is $\pm 4.2 + L/200$ μm, where L is is specified in millimeters and is the length scale over which measurements are taken. The width of a petal is its primary dimension, and therefore the optical edge is mainly concerned with deviations in the y (i.e. perpendicular to its length) direction. Since the test edge is a sinusoid with a peak-to-peak magnitude of 20 mm, L is also defined as 20 mm. Therefore, per the manufacturer, the accuracy of the machine is 4.3 μm. The prototype segments were held flat with a vacuum table during measurement. This reduces error in the MicroVu measurement by ensuring the entire length of edge is in focus. The combined repeatability of the machine and mounting arrangement were verified by measuring each segment 14 times in sequence. The segment was removed from the vacuum table and re mounted after the 5th, 8th, and 11th measurement. Therefore, the sequence included both repeatability errors in the machine and repeatability in mounting the edges for measurement. The 14 measurements were compared by plotting each against their combined average, as shown for

Table 10: Total number and percentage of data points that lie outside of 4.3 μm away from a mean value of 14 measurements of each segment.

	SN04	SN05	SN06	SN07	SN08	SN09
# of Data Points	97	48	30	39	49	33
% of Data Points	0.07%	0.04%	0.02%	0.03%	0.04%	0.02%

SN04 in Figure 27. A measure if the machine is repeatable within the manufacturer limits can be found by determining the percentage of data points that lie further than 4.3 μm away from the average. This information is presented in Table 10. Of all cases, the worst was SN04 for which only 0.07% of all data points fell outside the tolerance range of the MicroVu. Each of the 14 measurements in a sequence contained 9,580 data points; therefore, there are 134,120 total data points considered for each segment (excepting SN04 which contains only 13 measurements due to a data collection error).
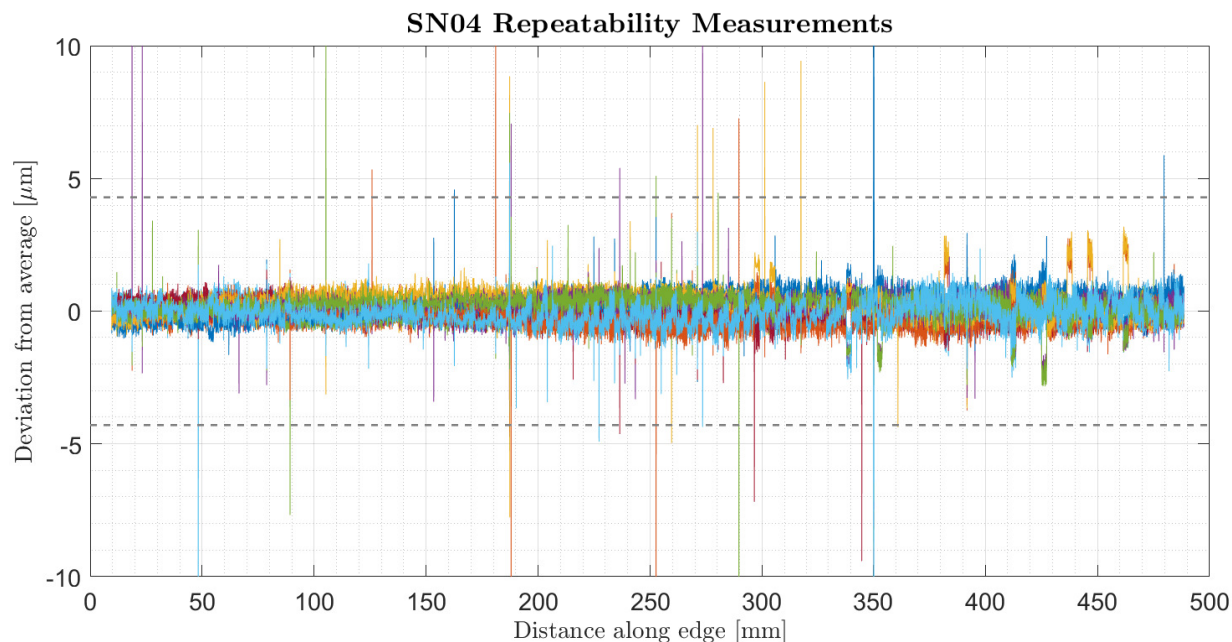
Figure 27: Repeatability measurement for SN09. The plot overlays a set of 14 measures taken to assess repeatability. The x axis is the average of all 14 data sets.

A.2   In-Plane Shape Results

The MicroVu is capable of measuring any arbitrarily shaped edge and returning an array of data points as a product. To verify in-plane shape, the collected data points were uploaded to MATLAB and compared to the design shape. A median filter was applied to reduce noise and a spline interpolator used to convert the data to a common grid with a data point every 50 μm. Lastly, an iterative RMS best fitting algorithm was applied to fit the measured data to the design without reference to other datums. Other errors such as a rotation of

amorphous metal relative to the CFRP can be adjusted when an edge segment is bonded to a petal.

Processed data for the six assembled edges can be found in Figure 28, while data that has been heavily filtered to remove features on spatial scales of <50 mm are shown in Figure 29. The plots show the measured deviation from the design across the entire 500 mm length of edge. As such, a perfectly formed edge would result in a line at x=0. Deviations are measured in microns along the y axis, which in this case has been defined as the direction perpendicular to a line formed by connecting the centers of an alignment hole and slot.

Qualitatively, each edge has a similar amount of high frequency noise with occasional high amplitude spikes; these spikes are thought to be contamination on the edge. The exception is SN04, which is noisier than the others because the amorphous metal used for SN04 was etched for a shorter amount of time as part of an experiment in etch timing, which left the terminal edge rougher. Table 11 lists statistical parameters of each part including the average absolute value, $|\mu|$, RMS of the deviation, and difference between as manufactured and post environmental test measurements. The maximum deviation between before and after measurements is only 0.7 μm, building confidence that in plane shape will remain consistent in the space environment. The data in Table 11 was generated from the plots shown in Figure 28.

All components met the in-plane shape requirement of ± 20 μm both before and after thermal cycling, excepting a few millimeters of length of SN05 and SN08 which strayed out of bounds. Note that the data presented here was collected after bend/release cycling, stowed thermal cycling, and deployed thermal cycling to +40/-100°C, but before deployed cycling to +105/-120°. Therefore, this data does not definitively show that edge shape is unaffected across all possible flight temperatures, but does build confidence that this is feasible.

Table 11: Average absolute value and RMS of all edges before and after environmental testing as compared to the design shape.

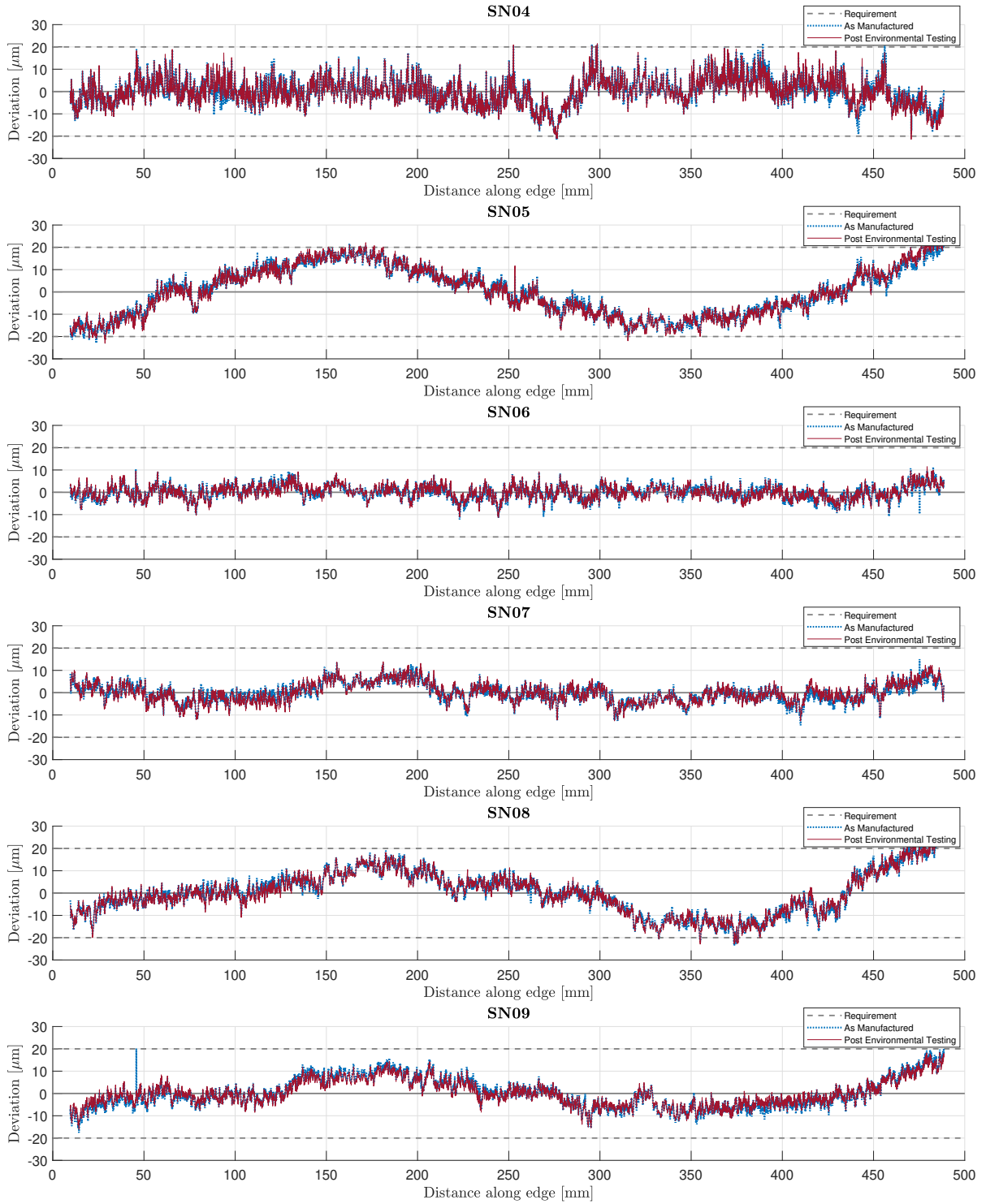|	SN	04	05	06	07	08	09
As Manufactured	$|\mu|$	4.7	9.6	2.4	3.5	7.6	4.7
	RMS	6.0	11.1	3.1	4.3	9.5	5.9
Post Environmental Testing	$|\mu|$	4.7	9.3	2.5	3.3	7.6	5.4
	RMS	6.0	10.7	3.1	4.2	9.4	6.6
Difference	$|\mu|$	0.0	0.3	0.1	0.2	0.0	0.7
	RMS	0.0	0.4	0.0	0.1	0.1	0.7

Figure 28: In-plane shape measurements for all six assembled edges before and after environmental testing.
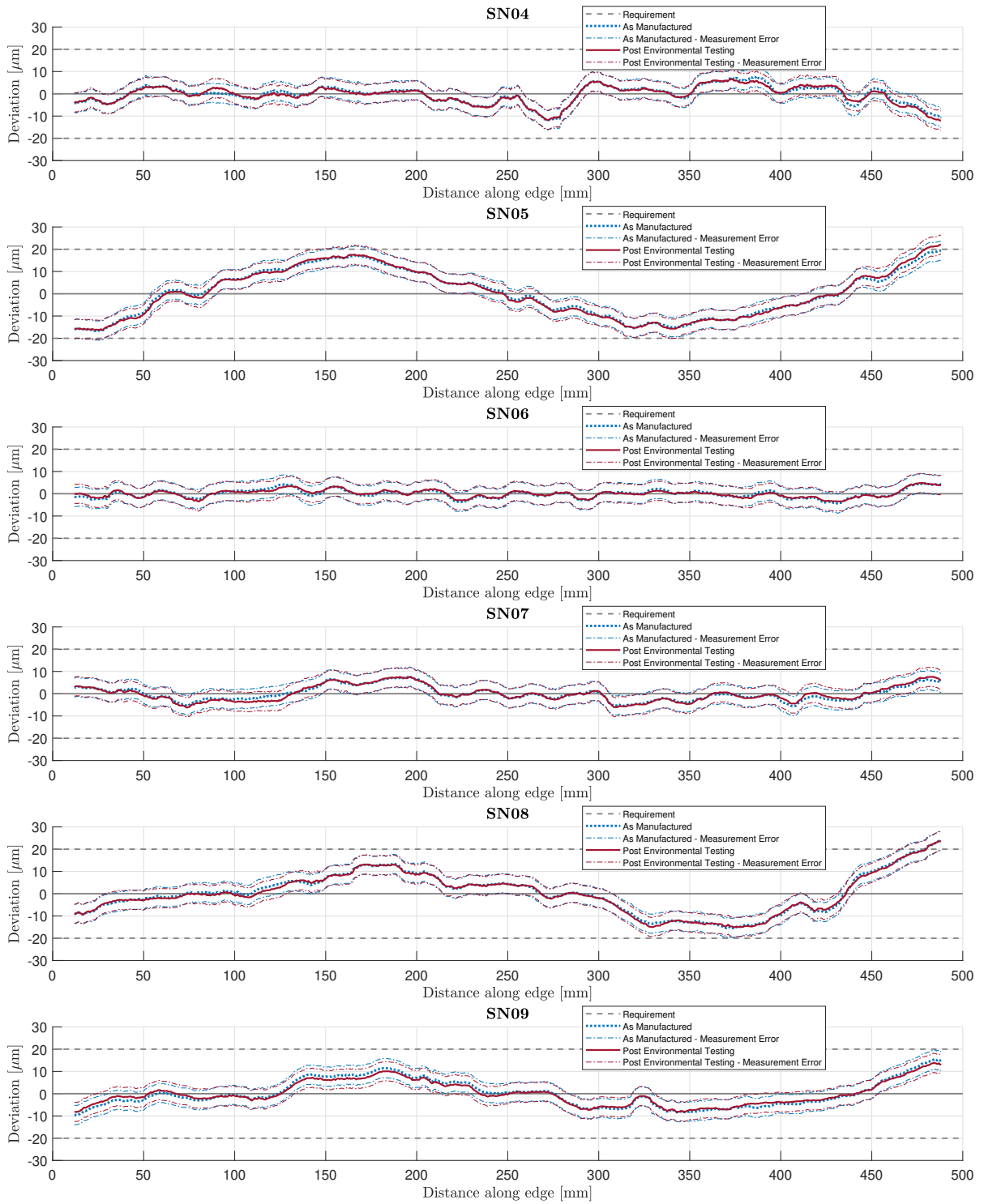
Figure 29: In-plane shape error measurements for all six assembled edges before and after environmental testing. Data has been filtered to remove features smaller then 50 mm.

Appendix B: Stowed Testing

The starshade is launched in the stowed configuration with the petals wrapped around the stowed perimeter truss as depicted in Figure 30a. The optical edge assemblies must mechanically survive the appropriate thermal ranges while furled to the stowed radius of 1.125 m. The same four point bending fixture described in Section 5.1.1 was used to define the radius of curvature throughout thermal cycling. This test was performed to determine mechanical limits of the bonded assembly and is not considered a driving case for scatter performance, as the temperature range over which the deployed edge assemblies were thermal cycled resulted in a delta temperature that was 50°C hotter and 119°C colder than the predicted on-orbit stowed starshade will experience. This assumption that stowed thermal cycle is not a scatter performance driver was verified by showing that the segments' scatter performance met the requirement after stowed thermal cycle testing. Scatter data for all segments after completion of all environmental testing is presented in Appendix D.

A detailed thermal model of the stowed starshade was used to derive test temperatures (Figure 30b). The model contained the Petal Launch Restraint and Unfurling System (PLUS), discrete petals covered with the optical shield, and the exposed CFRP structural edge. It was assumed that the stowed starshade spins at a minimum of 1 RPM to equalize temperatures symmetrically around the structure. Various orientations of the stowed system were studied across two relevant altitudes. The altitudes studied were 500 km, just after launch fairing is released and Earth albedo is a significant source of heat, and far-Earth, when Earth albedo is negligible.

The worst case mechanical test was that which resulted in failure of the bond line. Early analysis results showed that the shear stresses were low in the bond line, however early testing showed that non-ideal bond conditions could lead to foil buckling, and ultimately failure of the bond line in peel. With this discovered, the worst case stowed thermal condition for the bond was determined to be when the edge was hot, with the foil in compression, where the thermal expansion of the already compressed metal foil can lead to a peel force causing separation in the adhesive bond line.

The hot case occurred with the sun illuminating the side of the starshade (from the left or right of Figure 30) at an altitude of 500 km and included Earth albedo effects. This configuration resulted in a maximum temperature of 55°C. The maximum test temperature was 60°C, for which small (roughly 12 mm scale) disbonds between the amorphous metal and epoxy were discovered on edges in which the amorphous metal foil was in in compression. Therefore, hotter temperatures were not tested, and a series of tests at lower temperatures were performed. The same issue did not occur when segments were cooled, irrespective of amorphous metal being in compression or tension.

Thermal surface treatments for the CFRP were investigated to reduce the hottest temperature the edge would experience while stowed. For the same spacecraft orientation with respect to the sun, but at a far Earth altitude, this resulted in a cold temperature of -46°C. The coldest test temperature was -56°C to establish a ten degree margin on the prediction. More work is required to understand the coldest temperature a stowed edge would see between launch and the petal deployment at L2, the answer to this being dependent on specific mission parameters including the Earth to L2 trajectory with respect to incident sun angle

on the starshade. However, as it was not the driving case for mechanical design, the worst case cold was not exhaustively explored. The analysis performed conservatively covered the hottest case, which drives the mechanical design.

Although all six assembled segments experienced stowed thermal cycle testing, the test temperatures and number of cycles varied based on previous results. The complete testing history of each segment is given in Appendix C. The stowed testing showed that the adhesion issues required a dedicated study. The effort is ongoing and much insight has been gained already on how to improve the bond line adhesion to the amorphous metal. This effort is scheduled for completion by the end of fiscal year 2020. Ultimately the requirement will be verified as a part of milestone 5b.
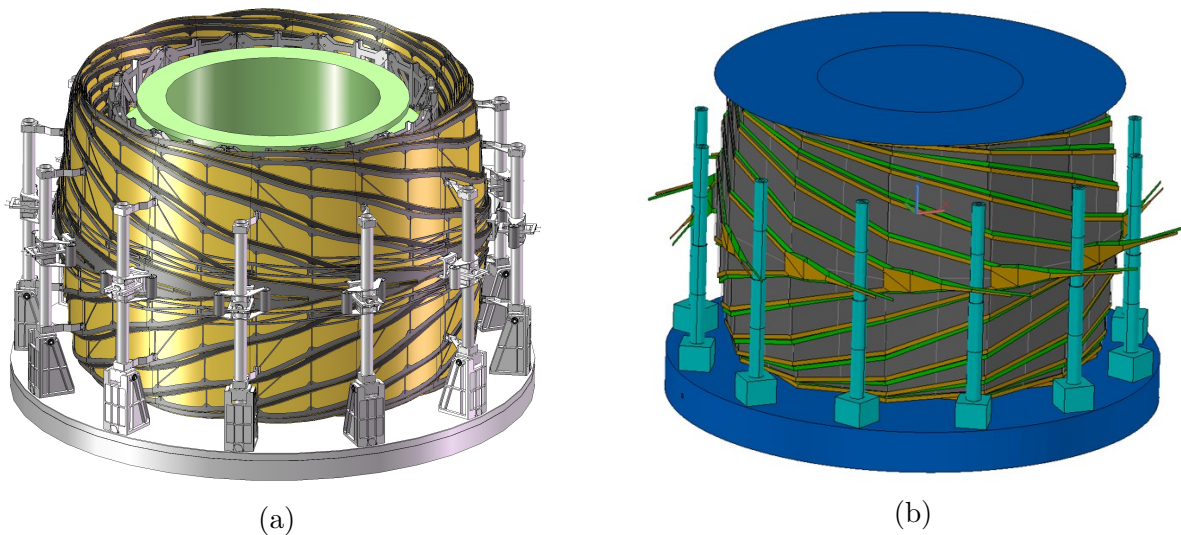
Figure 30: (a) CAD rendering of the stowed starshade along with (b) the analogous thermal model.

Appendix C: Complete Test History

The testing history of each segment is somewhat complex due to mechanical stability challenges encountered along the way and potential solutions. Table 12 provides a listing of the number of thermal cycles and test temperature for each of the six segments. Note that each line indicates a seperate test. For example SN05 performed 10 deployed thermal cycles from +40/-100°C and 50 cycles from +105/-125°C

Table 12: History of test sequences for all segments. All test temperatures are in °C

	Bend and Release Cycles	Deployed Thermal Cycles T_{max} / T_{min} / #	Stowed Thermal Cycles T_{max} / T_{min} / #
SN04	10	40 / -100 / 10	50 / -40 / 5 60 / 23 / 1
SN05	10	40 / -100 / 10 105 / -125 / 25	50 / -40 / 5 60 / 23 / 1 30 / -56 / 5
SN06	10	40 / -100 / 5 105 / -125 / 50	34 / 23 / 5 34 / -56 / 2
SN07	10	40 / -100 / 5 105 / -125 / 25	34 / 23 / 5 34 / -56 / 2
SN08	10	40 / -100 / 5 105 / -125 / 25	34 / 23 / 5 34 / -56 / 2
SN09	10	40 / -100 / 5	50 / -40 / 5

Appendix D: Edge Scatter Measurements

The following plots show the SAS measurements of scattered light for all assembled edge segments and reference coupons. Segments 4-9 are shown after environmental testing.

SAS Measurement - SN06 10/07/2019

SAS Measurement - SN07 10/23/2019

Coupon SAS Measurements
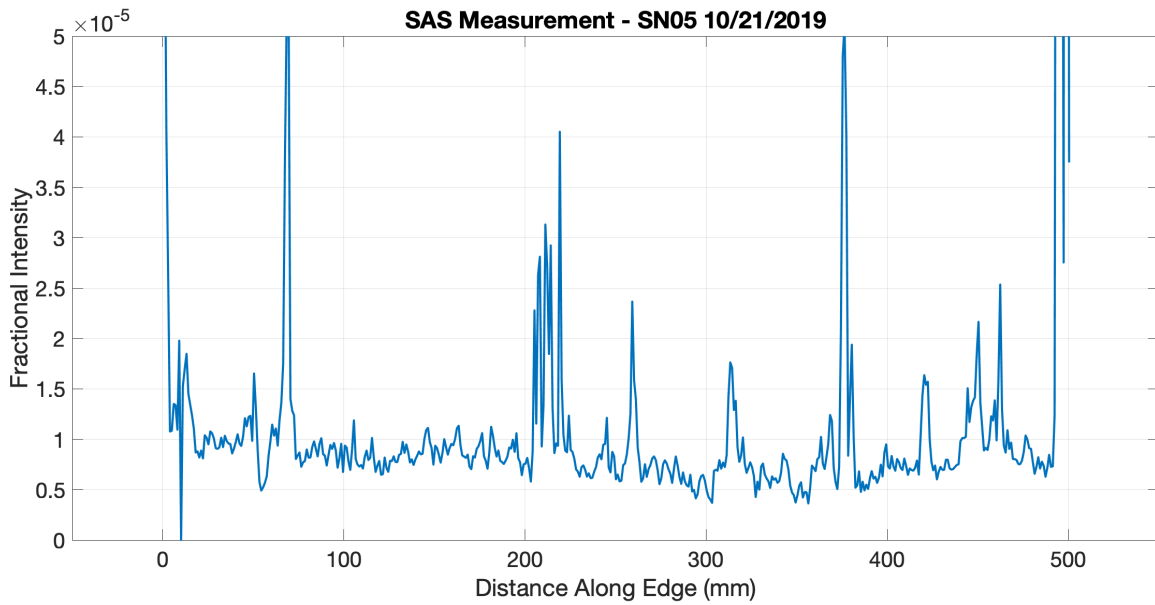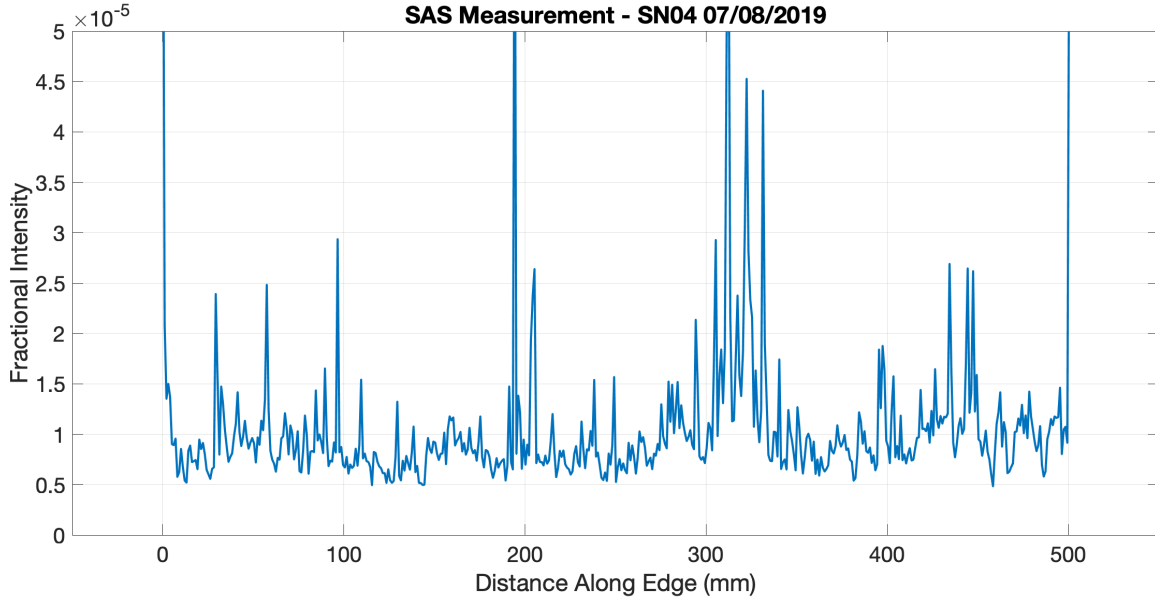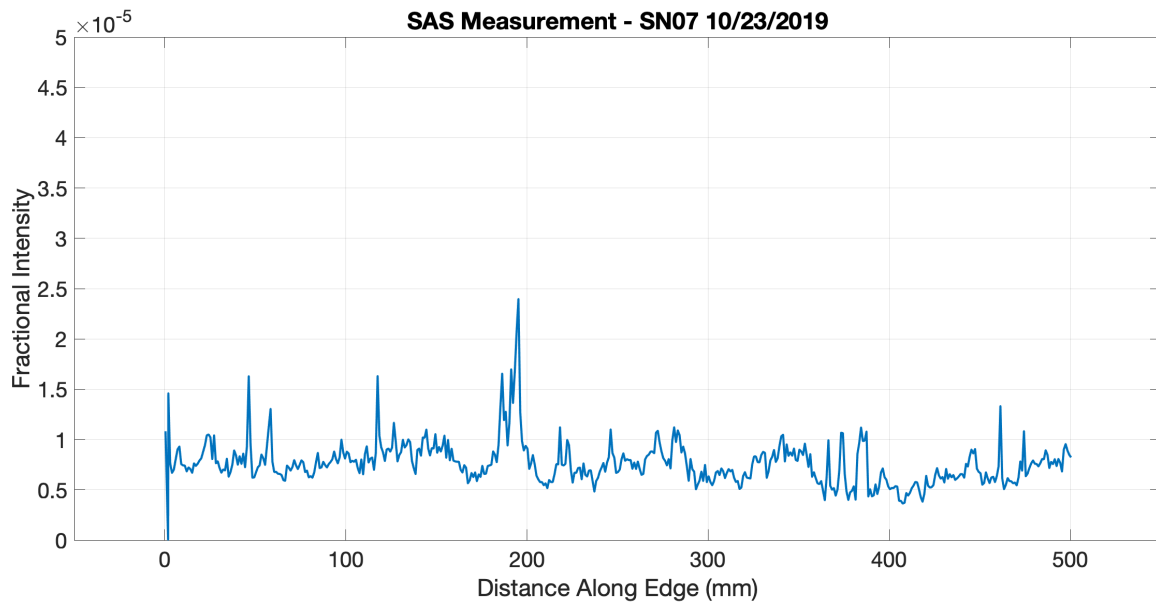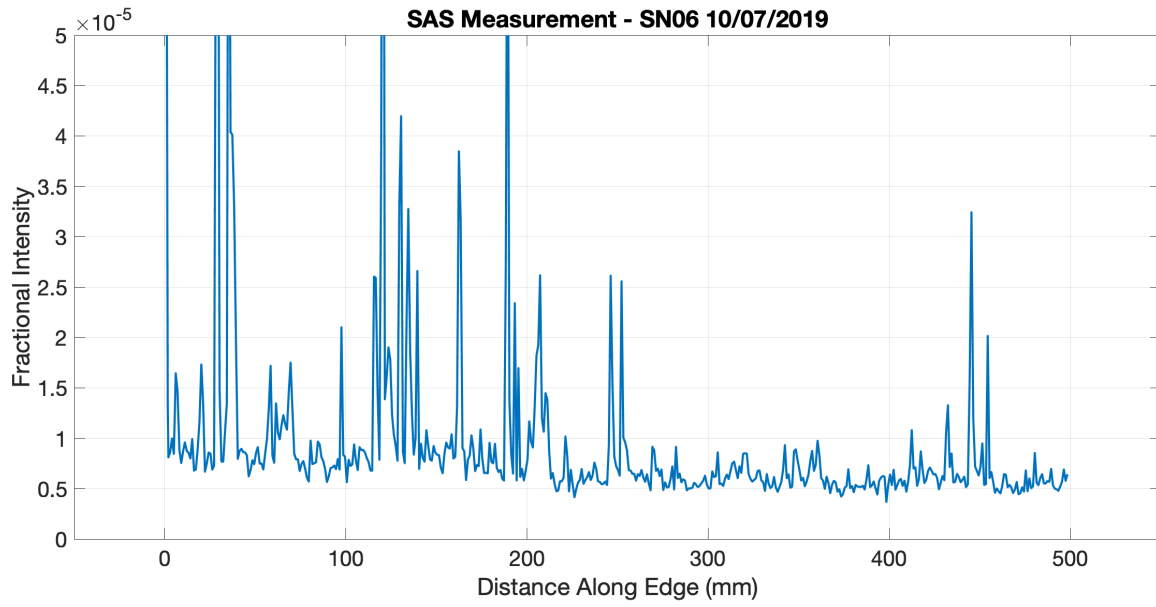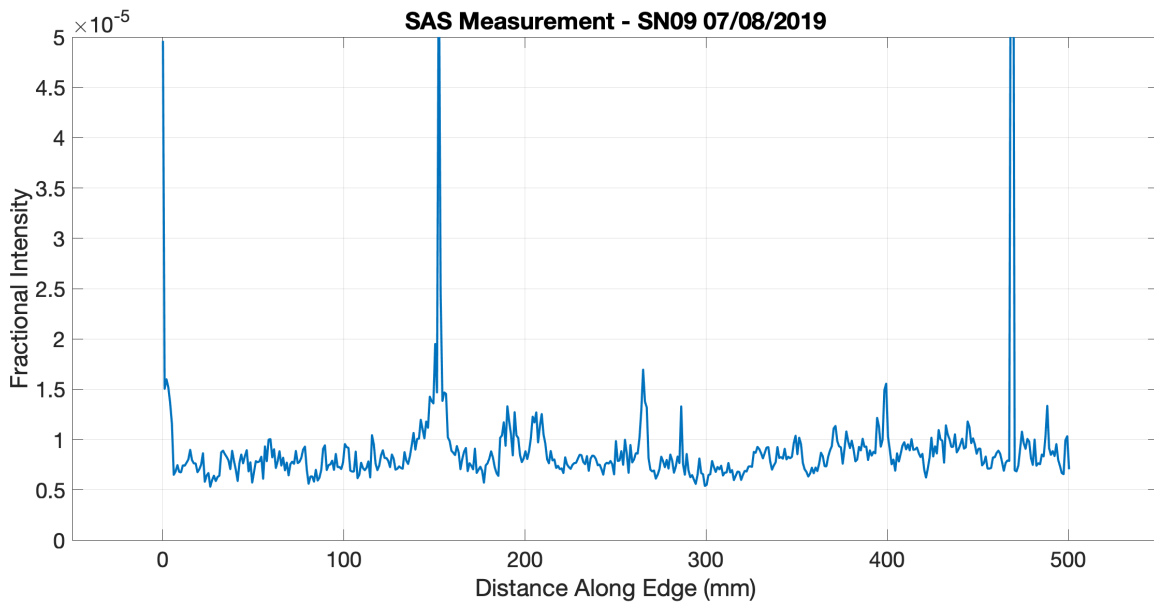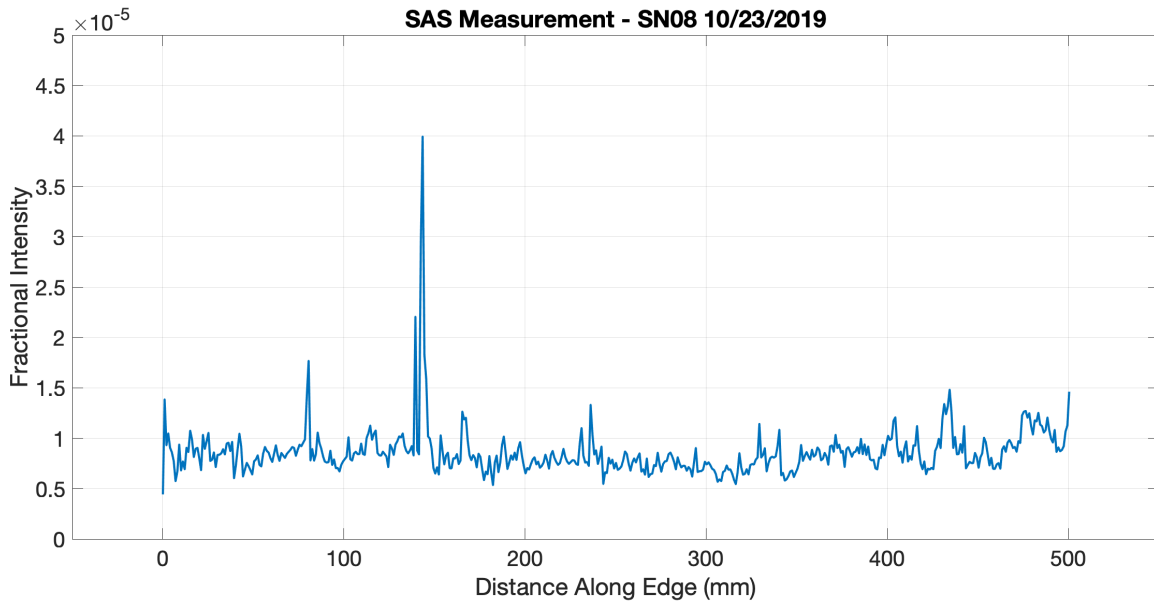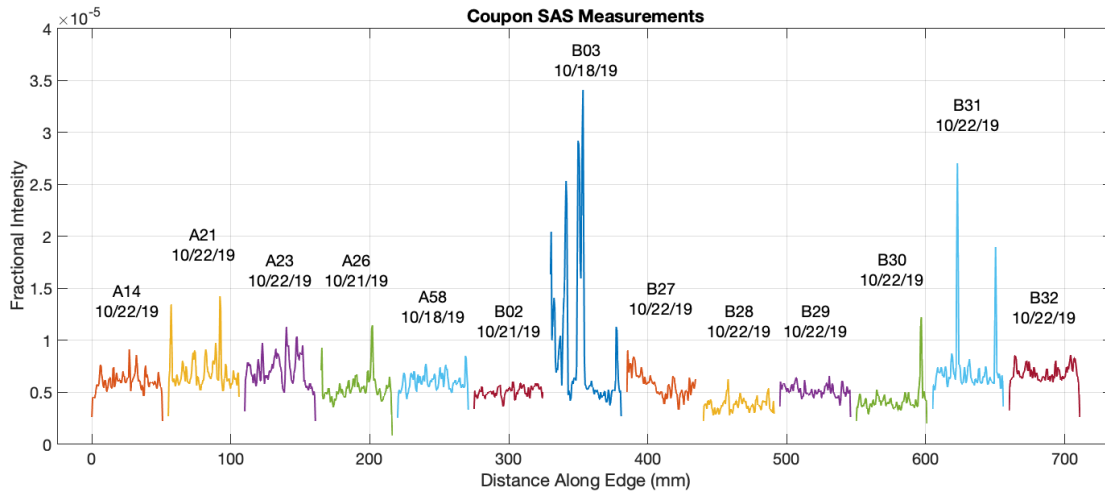
Appendix E: Pre- and Post-Environmental Testing Scatter Measurements

Segments 6, 7, and 8 were measured before any environmental testing and after all testing had completed. The data shown here were used to reach the conclusion that thermal and deployment cycles did not adversely affect the edge scattering properties. Each edge was measured 3 times prior to environmental testing; here we plot the average of the measurments. The segments were measured once after environmental testing.
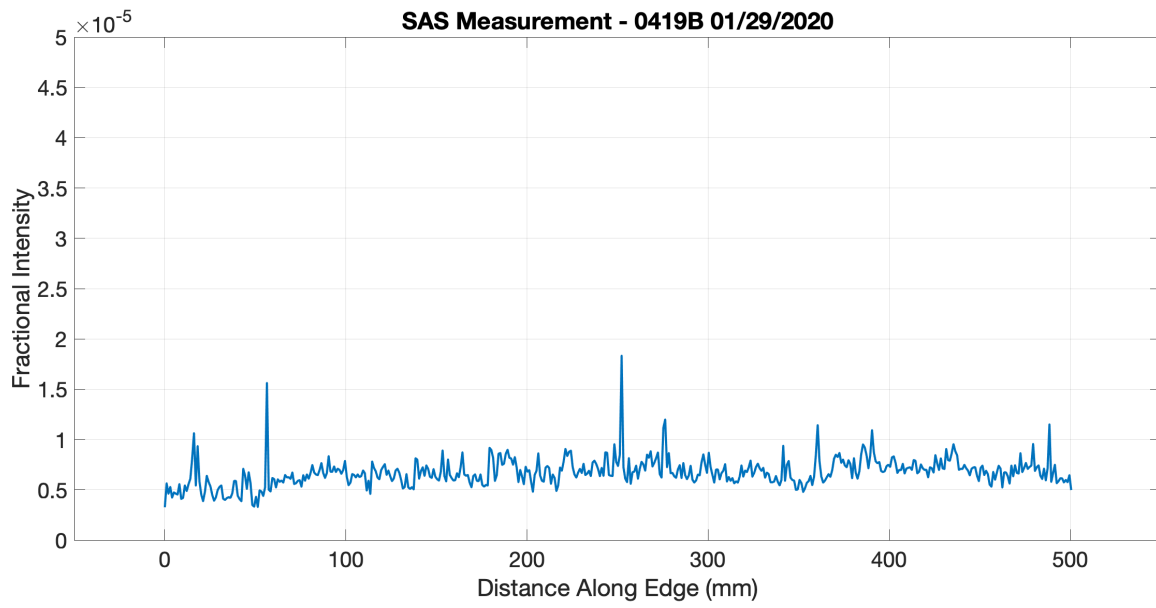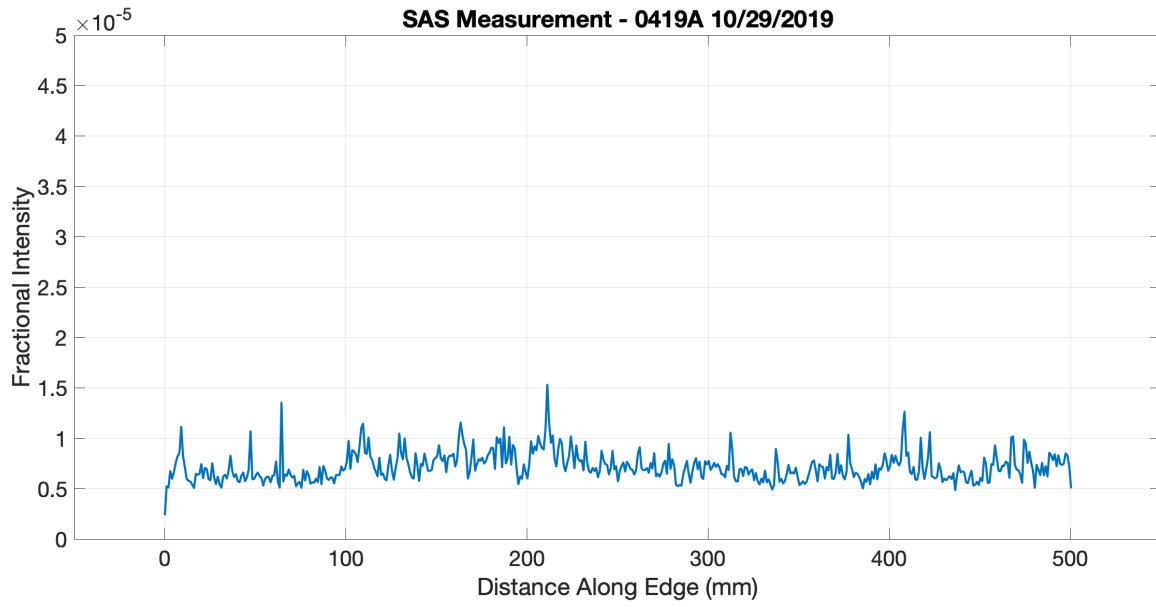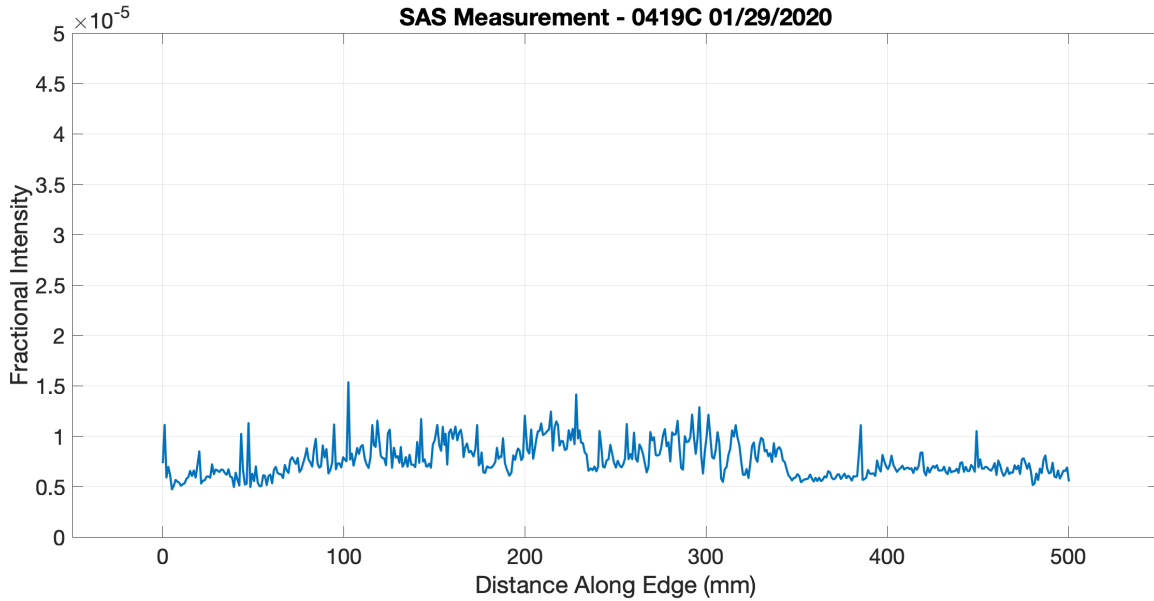

SN06 Before and After Environments
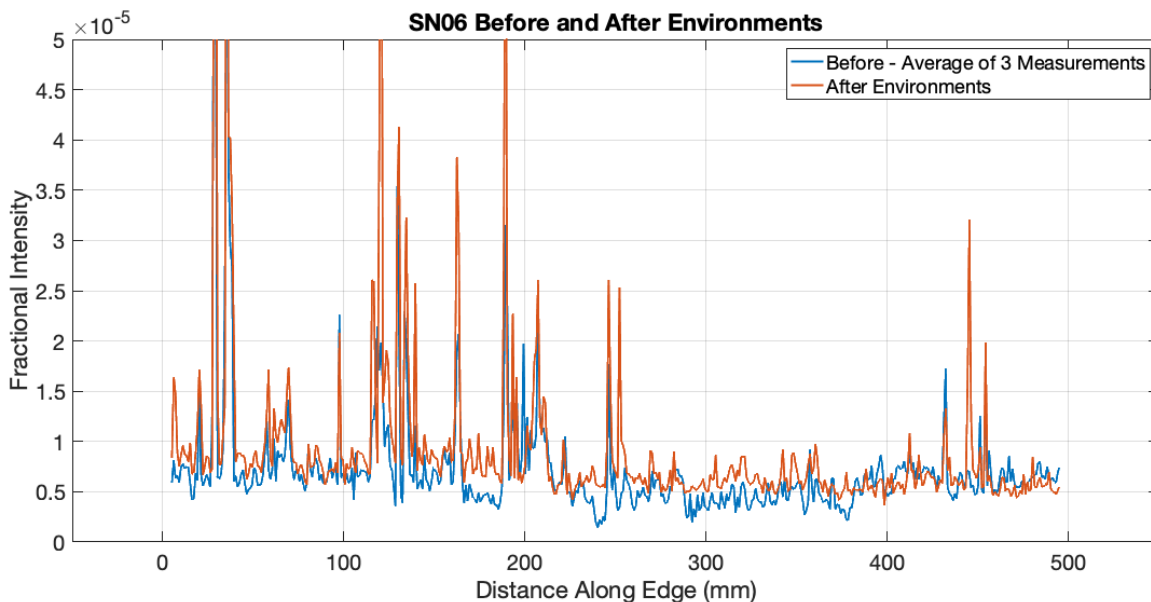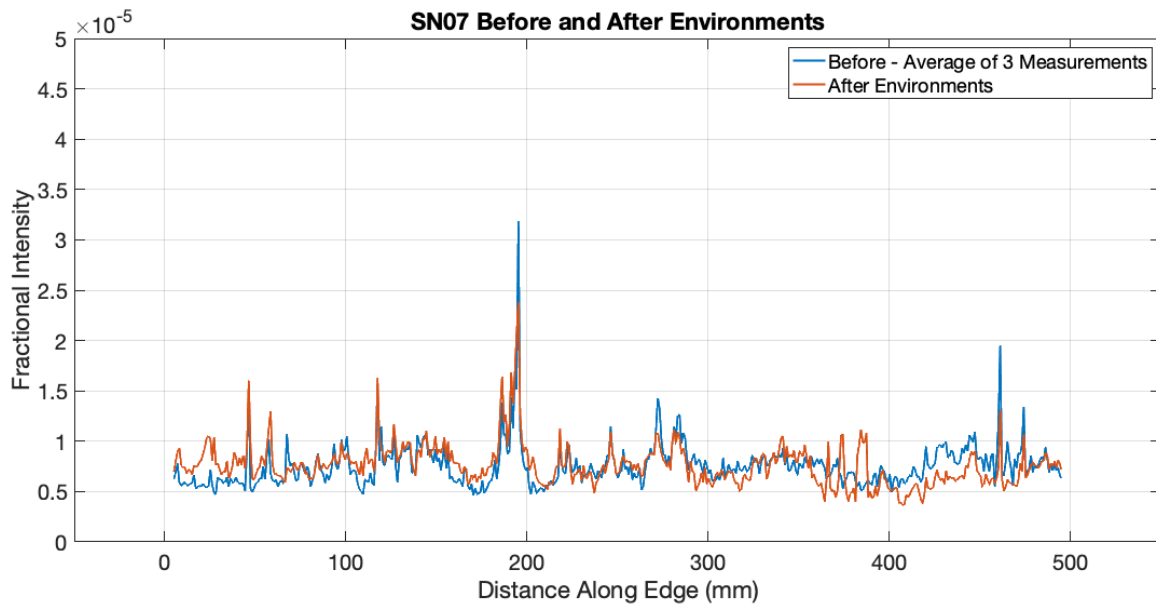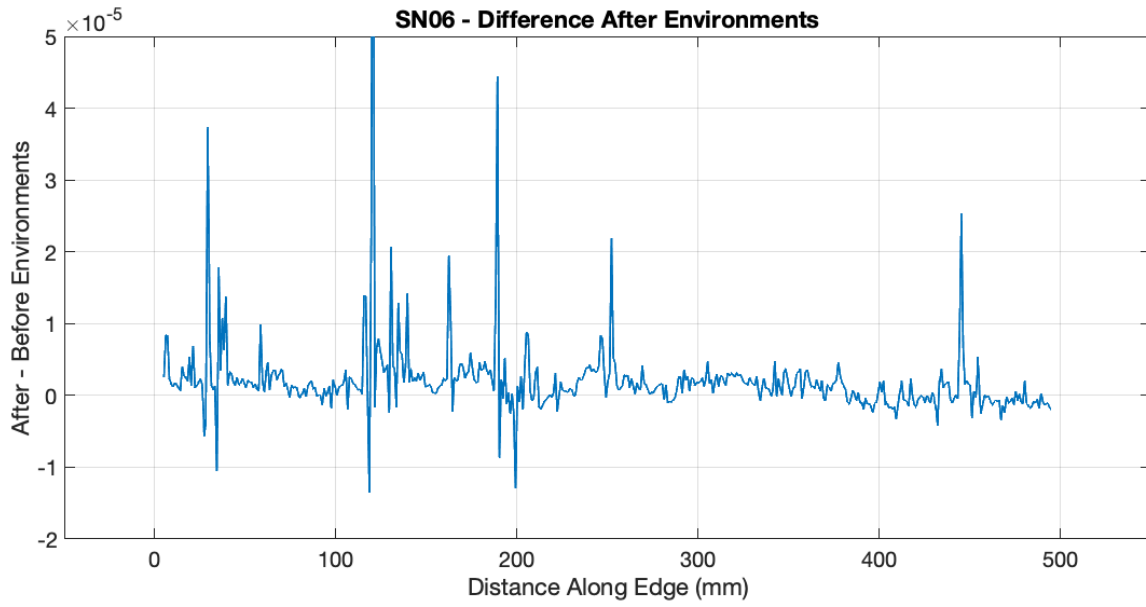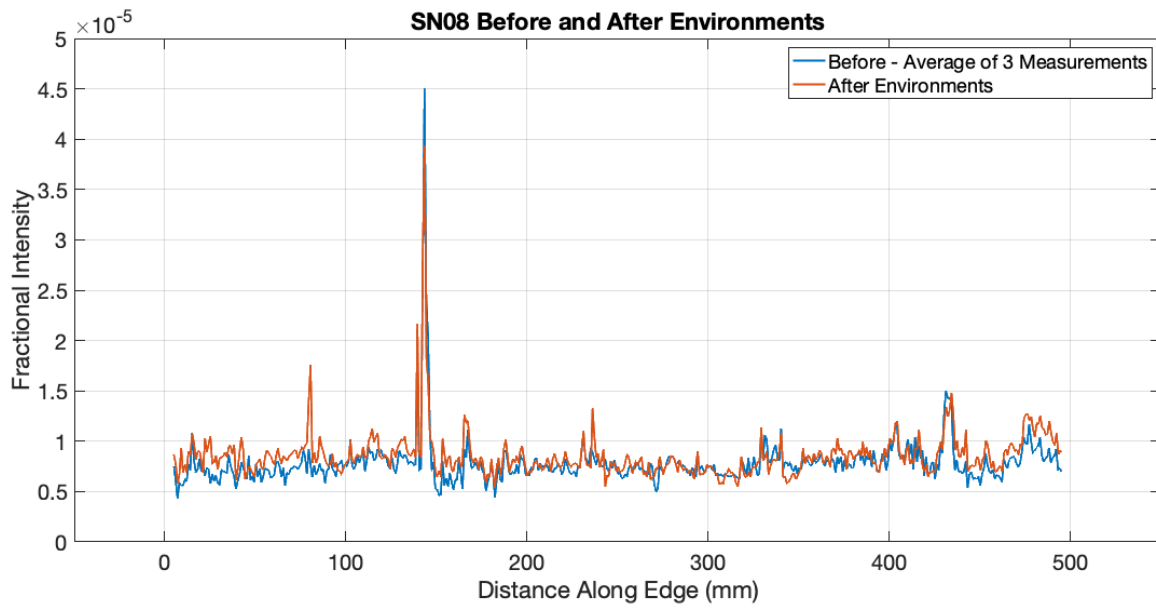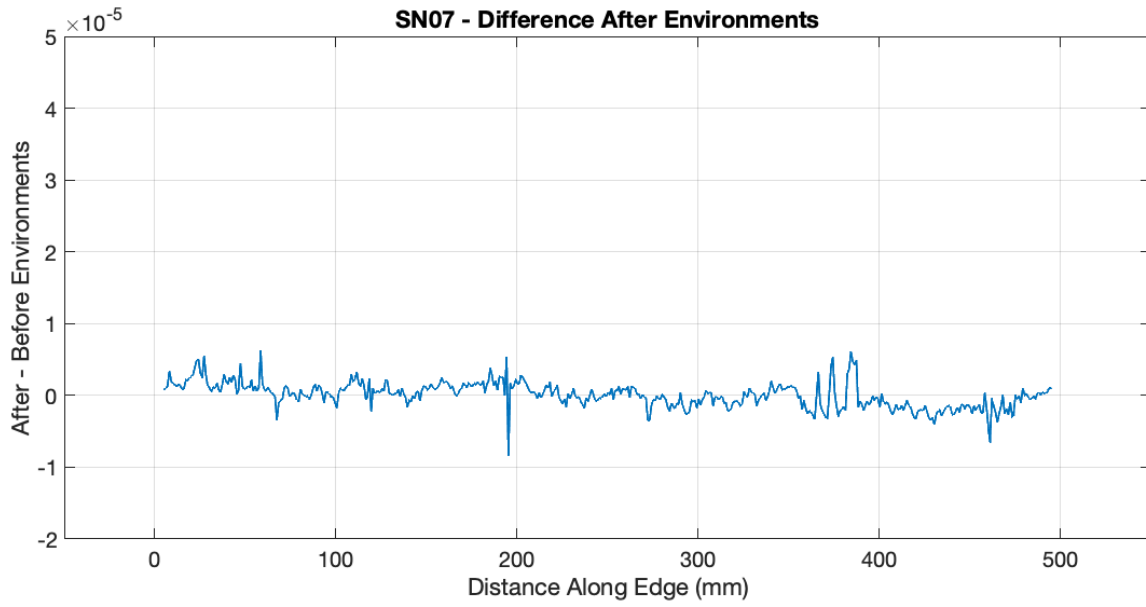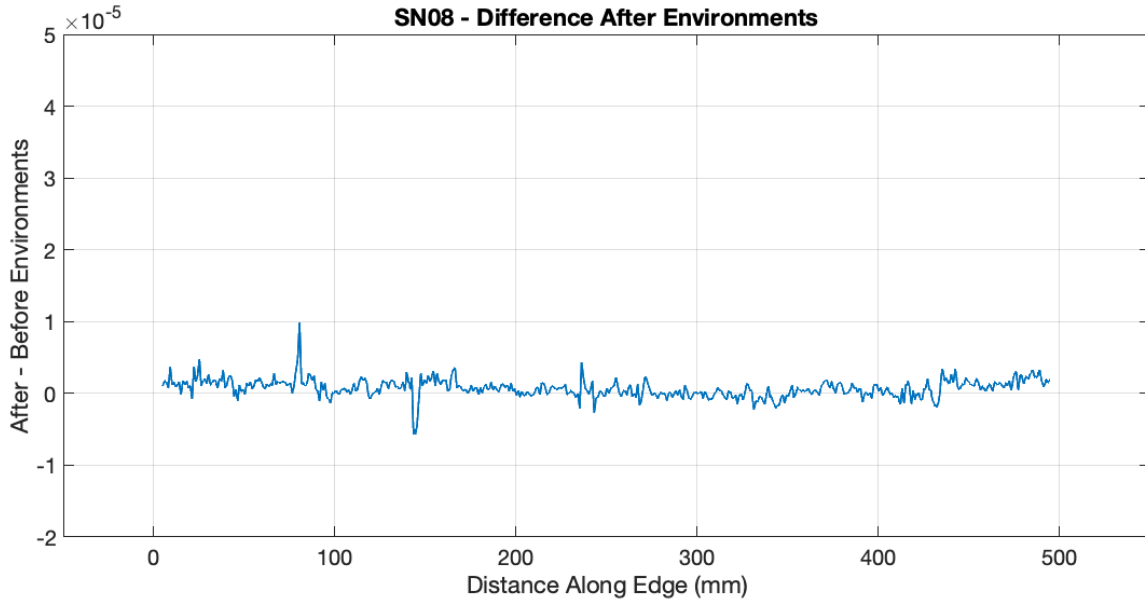
Appendix F: Unmounted Segment Data

It is possible that the mounted segment geometry (Figure 14a) increases edge scatter relative to the terminal edge, independent of any possible damage or contamination of the edge during the mounting process. To test this, we compare the SAS scatter measurements of three mounted segments (SN06, 07, 08, prior to environmental testing) to three unmounted segments. Scatter plots for the mounted segments are shown in Appendix E, while the data for the three unmounted segments, 0419A, B, and C, are shown below.The average scatter ratio (mounted / unmounted) is 1.17, while the average ratio of the median scatter (which should be insensitive to the large peaks) is 1.14. We conclude that mounts may indeed be contributing to the scatter. Recall that from Table 4 that we found the mounted segments to be roughly 40% brighter than the coupons, while here we find that the mounted segments are about 14-17% brighter than unmounted segments. Thus, it is possible that the mounting geometry is itself accounting for almost half of the additional scatter relative to the coupons. This does not mean that the same additional scatter will be seen on orbit – it could simply be a matter of our overall instrument geometry. It is also possible that the unmounted segments were of slightly better overall quality than the mounted ones. We will investigate in more detail in future work.

SAS Measurement - 0419A 10/29/2019

SAS Measurement - 0419B 01/29/2020

SAS Measurement - 0419C 01/29/2020

Appendix G: Estimates of Scatter from Coupon and Segment Mounts

We address the contributions of coupon holders to the measured scatter. The coupons are mounted in their holders (Figure 18) with the working edge 7 mm proud of their two-piece shells. To study the sensitivity to the edge/shell separation, we adjusted a coupon in its mount, increasing the edge-to-shell separation up to 12 mm. We captured the specular scatter by measured the scatter in the MAS over a range of $-10° < \theta < 10°$ and for the range of observational Sun angles $40° < \phi < 85°$. We also made repeated measurements of a mounted coupon over the course of two days (Figure 31). The shell separation test (Figure 32) showed no clear trend indicating sensitivity to the edge offset from the shell. We conclude from this test that the coupon holder contribution to the scattered light level is at most a few percent.
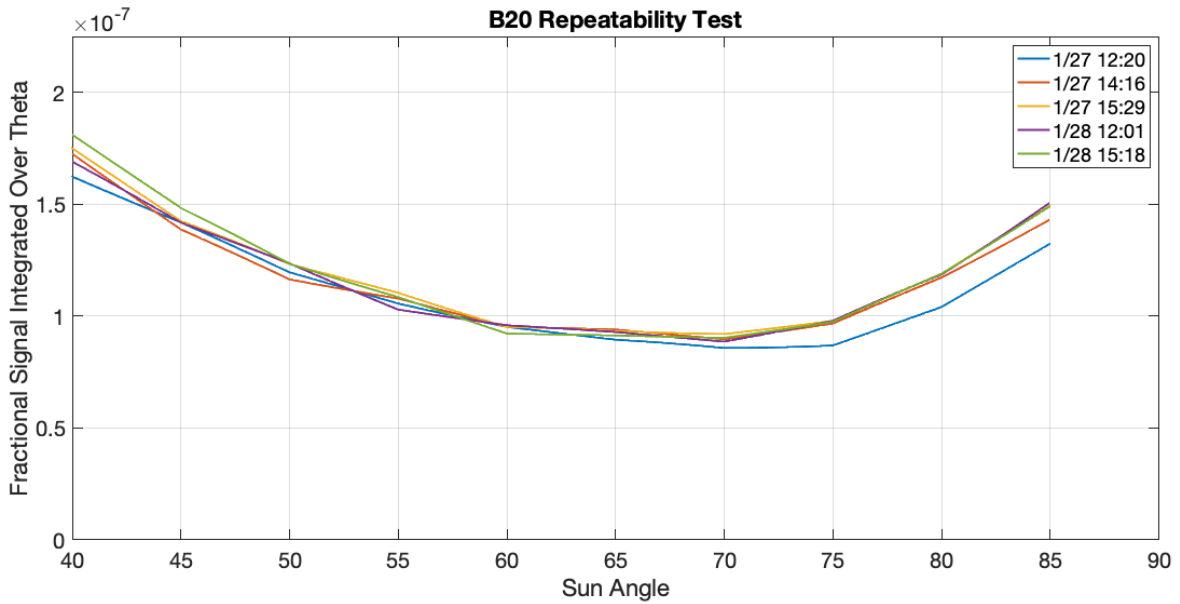
Figure 31: MAS coupon stability measurements. The coupon was place in the MAS for 24 and measured 5 times. THe coupon was neither moved nor touched during this time.
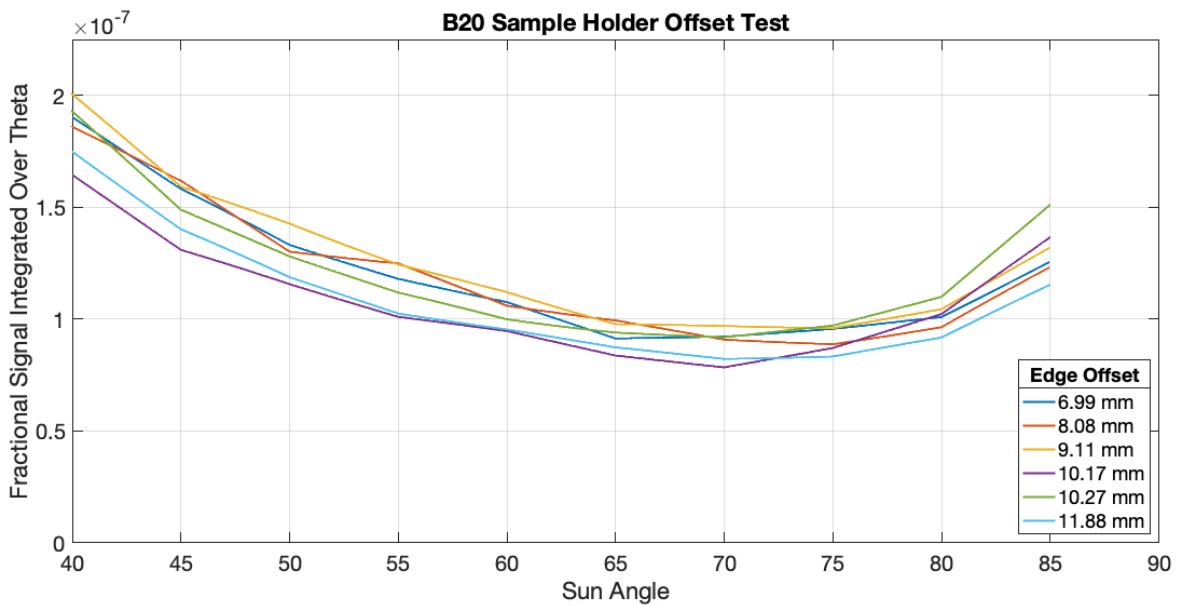

Figure 32: The coupon was adjusted in its mount to increase the distance between the working edge and the mount shell from the 7 mm nominal separation to 12 mm over a 24 hours period.